OXFORD

Human Molecular Genetics, 2018, Vol. 27, No. 10 1675–1695

doi: 10.1093/hmg/ddy074
Advance Access Publication Date: 1 March 2018
Original Article

ORIGINAL ARTICLE

PITX2 deficiency and associated human disease: insights from the zebrafish model

Kathryn E. Hendee[1,2], Elena A. Sorokina[1], Sanaa S. Muheisen[1], Linda M. Reis[1], Rebecca C. Tyler[1], Vujica Markovic[3,4], Goran Cuturilo[3,5], Brian A. Link[2,6] and Elena V. Semina[1,2,6,*]

[1]Department of Pediatrics and Children's Research Institute, Medical College of Wisconsin and Children's Hospital of Wisconsin, Milwaukee, WI 53226, USA, [2]Department of Cell Biology, Neurobiology, and Anatomy, Medical College of Wisconsin, Milwaukee, WI 53226, USA, [3]Faculty of Medicine, University of Belgrade, Serbia, [4]Clinical Centre of Serbia, University Eye Hospital, Belgrade, Serbia, [5]Department of Medical Genetics, University Children's Hospital, Belgrade, Serbia and [6]Department of Ophthalmology, Medical College of Wisconsin, Milwaukee, WI 53226, USA

*To whom correspondence should be addressed at: Department of Pediatrics, Medical College of Wisconsin, 8701 Watertown Plank Road, Milwaukee, WI 53226, USA. Tel: +1 4149554996; Fax: +1 4149556329; Email: esemina@mcw.edu

Abstract

The *PITX2* (paired-like homeodomain 2) gene encodes a *bicoid*-like homeodomain transcription factor linked with several human disorders. The main associated congenital phenotype is Axenfeld-Rieger syndrome, type 1, an autosomal dominant condition characterized by variable defects in the anterior segment of the eye, an increased risk of glaucoma, craniofacial dysmorphism and dental and umbilical anomalies; in addition to this, one report implicated *PITX2* in ring dermoid of the cornea and a few others described cardiac phenotypes. We report three novel *PITX2* mutations—c.271C > T, p.(Arg91Trp); c.259T > C, p.(Phe87Leu); and c.356delA, p.(Gln119Argfs*36)—identified in independent families with typical Axenfeld-Rieger syndrome characteristics and some unusual features such as corneal guttata, Wolf-Parkinson-White syndrome, and hyperextensibility. To gain further insight into the diverse roles of *PITX2/pitx2* in vertebrate development, we generated various genetic lesions in the *pitx2* gene via TALEN-mediated genome editing. Affected homozygous zebrafish demonstrated congenital defects consistent with the range of *PITX2*-associated human phenotypes: abnormal development of the cornea, iris and iridocorneal angle; corneal dermoids; and craniofacial dysmorphism. In addition, via comparison of *pitx2*^{M64*} and wild-type embryonic ocular transcriptomes we defined molecular changes associated with *pitx2* deficiency, thereby implicating processes potentially underlying disease pathology. This analysis identified numerous affected factors including several members of the Wnt pathway and collagen types I and V gene families. These data further support the link between PITX2 and the WNT pathway and suggest a new role in regulation of collagen gene expression during development.

Received: December 6, 2017. **Revised:** January 30, 2018. **Accepted:** February 26, 2018

Introduction

Paired-like homeodomain 2 [*PITX2* (MIM 601542)] is a *bicoid*-like homeodomain transcription factor first identified as the cause of Axenfeld-Rieger syndrome (ARS), type 1 [(MIM 180500)], an autosomal dominant developmental disorder characterized by the combination of specific ocular and systemic defects (1–3). The typical ocular feature, often referred to as Axenfeld-Rieger anomaly, includes posterior embryotoxon, iris hypoplasia, iris processes, and corectopia/polycoria and is associated with a ∼50% risk of developing glaucoma (2,4). Systemic features include maxillary hypoplasia, micro- and hypodontia, redundant periumbilical skin and more rarely umbilical hernia, omphalocele, anal anomalies, hypospadias, Meckel's diverticulum and other defects (2,3,5,6). Several reports also implicate *PITX2* in heart phenotypes including atrial fibrillation (AF) (7–11). In addition, one paper describes a family with a rare phenotype of ring dermoid of the cornea [MIM180550] carrying a pathogenic variant in *PITX2* (12).

PITX2 has multiple isoforms, with three main transcripts seen in mammalian species: *PITX2-A, -B* and *-C* (13,14). The isoforms are generated by alternative splicing and/or use of different promoters and thus have diverse N-terminal regions; however, all three have identical homeodomain and C-terminal sequences. Most *PITX2* mutations affect the homeodomain and C-terminal regions (via deletions, splicing or missense alleles) and result in complete or partial loss of function due to their disruption of all known PITX2 isoforms (3,6,13). Evident null alleles (complete gene deletions) support *PITX2* haploinsufficiency as a mechanism of ARS (1,3,6,15). Human development appears to be highly sensitive to PITX2 dosage, as mutant proteins that retain limited wild-type activities seem to associate with milder phenotypes (16–18); in addition, increased transactivation capacity observed in some PITX2 mutants indicate that excessive PITX2 activity may also be harmful to proper development (6,19,20).

The normal developmental pathways downstream of Pitx2 are largely unknown; consequently, the mechanisms by which *PITX2* mutations result in the variable Axenfeld-Rieger phenotype have yet to be fully elucidated. Dickkopf 2 (*Dkk2*), an extracellular antagonist of canonical Wnt-β-catenin signaling, was identified as the first downstream target of Pitx2 involved in periocular mesenchyme/anterior segment development (21). Pitx2 has also recently been shown to be required for normal *Tfap2b* expression within the neural crest (22). In non-ocular tissues, PITX2 activates transcription of distal-less homeobox 2 (*Dlx2*) within the dental epithelium during tooth development (23). When considering co-factors of Pitx2, the most relevant protein-protein interaction to date is that of Pitx2 and forkhead box transcription factor C1 (Foxc1), another key gene implicated in ARS, type 3 [MIM 602482] (24,25). PITX2 and FOXC1 are co-expressed in distinct periocular mesenchyme cells during multiple time points in ocular development, and both proteins localize to a common subnuclear compartment (26). In addition, the two proteins were shown to physically interact through immunoprecipitation assays; this interaction was found to rely on the PITX2 homeodomain and a PITX2-binding domain within the C-terminal activation domain of FOXC1 (26).

The function of PITX2 is highly conserved during vertebrate development. Mice homozygous for *Pitx2* null or hypomorphic alleles are embryonic lethal and display ARS-related anomalies including arrest in tooth development, abnormal eye placement, absence of ocular muscles and abnormal anterior segment structures, among numerous other abnormalities (27–30). In addition, heterozygous *Pitx2* mutant mice previously considered unaffected have recently been shown to manifest the ocular features of ARS (31). Vertebrate conservation of PITX2 function also extends to zebrafish where two isoforms, *pitx2a* and *pitx2c* (orthologs of *PITX2A* and *PITX2C*, respectively), have been identified. Human and zebrafish ocular structures show significant anatomical similarities while also displaying a few differences. With respect to anterior segment structures, zebrafish and human corneas both display a stratified multilayer epithelium, a stroma of orthogonally-arranged collagen fibrils, and a monolayer endothelium (32–34); the remaining human corneal layers, Bowman's and Descemet's membranes, may not be present in zebrafish according to one recent paper (35). Zebrafish show a strikingly similar normal intraocular pressure (IOP) range to mammalian species, including humans (34). However, unlike in the human eye where aqueous humor is produced by the ciliary body and drained through the trabecular meshwork and Schlemm's canal that extend circumferentially around the base of the cornea, aqueous humor production and drainage in zebrafish are managed by specialized structures located in the iridocorneal angle. Aqueous humor is produced in the dorsal angle of the eye by secretory cells of the non-pigmented ciliary epithelium, while drainage occurs in the ventral angle through the canalicular drainage network (32,36). Like humans, anterior segment structures in zebrafish receive contributions from diverse embryonic lineages (surface ectoderm, head mesoderm, neural crest and neuroectoderm), with *pitx2* showing conserved robust expression in the neural crest-derived periocular mesenchyme. Normal expression of *pitx2* in embryonic tissues is critical to their development as complete morpholino-mediated knockdown of *pitx2* results in ocular, craniofacial, and other defects (37). Recent publications also demonstrate the presence of a gross developmental phenotype in a zebrafish mutant line (38), as well as mild ocular defects in zebrafish mutants with deletion of the upstream regulatory regions of *pitx2* that were previously shown to be conserved with humans (14,39).

In this manuscript we describe three novel dominant *PITX2* mutations identified in three independent ARS families and highlight the variability of the associated phenotypes, both in terms of the severity of classic features as well as the occurrence of additional sporadic systemic defects. To gain further insight into the diverse roles of *PITX2/pitx2* in vertebrate development and the mechanisms of associated variable phenotypes, we established permanent *pitx2*-deficient zebrafish lines via transcription activator-like effector nucleases (TALEN)-mediated genome editing and present their characterization with a focus on ocular abnormalities observed in homozygous animals. In addition, by comparing *pitx2*$^{-/-}$ and wild-type embryonic eye transcriptomes, we identify molecular changes associated with pitx2 deficiency that potentially underlie disease pathology.

Results

Identification of novel PITX2 mutations in human patients

Screening of *PITX2* and *FOXC1* in patients with ARS identified three novel causative mutations in *PITX2*: c.271C > T, p.(Arg91Trp) (Family 1); c.259T > C, p.(Phe87Leu) (Family 2); and c.356delA, p.(Gln119Argfs*36) (Family 3) (Table 1, Fig. 1). The first two mutations affect the homeodomain region of the protein, and the last one results in premature truncation and deletion of a large

Table 1. Summary of clinical and genetic features observed in Axenfeld-Rieger syndrome patients in this study

Patient	Eye	Dental	Umbilicus	Other features	Race/ ethnicity	DNA effect[a]	Protein effect	Functional prediction[b]	Family hx
1A	ARA, GL, aniridia partialis, coloboma	DA	RU	MH, BN, ptosis	Caucasian (Serbia)	c.271C>T	p.(Arg91Trp)	Damaging by 5/5 (S, PP, MT, MA, F)	Yes
1B	ARA, corneal guttata	DA	Unk	MH, BN	Caucasian (Serbia)	c.271C>T	p.(Arg91Trp)	Damaging by 5/5 (S, PP, MT, MA, F)	Mother of 1A
1C	ARA, GL, CA	DA	Unk	MH	Caucasian (Serbia)	c.271C>T	p.(Arg91Trp)	Damaging by 5/5 (S, PP, MT, MA, F)	Grandmother of 1A
2A	ARA, GL	Unk	Unk	MH	Caucasian (Serbia)	c.259T>C	p.(Phe87Leu)	Damaging by 5/5 (S, PP, MT, MA, F)	Yes
2B	ARA, GL	Unk	RU	MH, BN, (MR, SZ)[c]	Caucasian (Serbia)	c.259T>C	p.(Phe87Leu)	Damaging by 5/5 (S, PP, MT, MA, F)	Son of 2A
3A	ARA, GL	HD, MD	RU, UH	mitral valve prolapse	Caucasian (USA)	c.356delA	p.(Gln119Argfs*36)	Premature truncation	Yes
3B	ARA, GL	HD, MD	UH	WPW, hyperextensibility	Caucasian (USA)	c.356delA	p.(Gln119Argfs*36)	Premature truncation	Son of 3A

ARA, Axenfeld-Rieger anomaly (any combination of posterior embryotoxon, iris processes, iris hypoplasia, and pupillary anomalies); BN, broad nasal bridge; CA, cataract; DA, dental anomaly; GL, glaucoma; HD, hypodontia; MD, microdontia; MH, maxillary hypoplasia; MR, mental retardation; RU, redundant umbilical skin; SZ, Seizures; UH, umbilical hernia; Unk, unknown.

[a]Numbering is relative to reference sequence NM_153427.2 where +1 is the A of the ATG initiation codon.

[b]5 prediction algorithms [SIFT (S), PolyPhen2 (PP), MutationTaster (MT), MutationAssessor (MA), FATHMM (F)] accessed through the Variant Effect Predictor (http://useast.ensembl.org/Homo_sapiens/Tools/VEP).

[c]MR and SZ felt to be due to neonatal asphyxiation, not *PITX2* mutation.

portion of the C-terminal region; even though all three mutations are novel, their expected functional effects are consistent with previously reported disease-associated alleles (Fig. 2). All three alleles are absent in over 250 000 general population alleles (gnomAD Browser). All three alleles co-segregated with the ARS phenotype in affected family members described below; no unaffected family members were available for testing. No other coding variants were identified in *PITX2*. Sequencing of *FOXC1* in all three probands identified two common [c.1139_1141dupGCG, p.(Gly380dup) and c.1359_1361dupCGG, p.(Gly456dup) at 16 and 25% allele frequency in the general populations, respectively] and one rare [c.1476_1481delGGCGGC, p.(Ala494_Ala495del) at 0.073% allele frequency] in-frame indels. Co-segregation studies were performed for the rare variant; however, all three met criteria to be classified as benign by ACMG/AMP (American College of Medical Genetics and Genomics/Association for Molecular Pathology) guidelines (40).

Patient 1A is an 8-year-old Caucasian male from Serbia diagnosed with ARS. He has bilateral typical ocular anomalies consisting of posterior embryotoxon, iris processes, iris hypoplasia and corectopia along with glaucoma diagnosed at 6 years of age. His left eye is more severely affected with partial aniridia and iris coloboma. Non-ocular anomalies include redundant periumbilical skin, dental defects, maxillary hypoplasia, broad nasal bridge, and ptosis (Fig. 1). His mother (Patient 1B) has posterior embryotoxon, iris hypoplasia, corneal guttata, dental defects, maxillary hypoplasia and a broad nasal bridge; no umbilical anomalies were noted. The patient's maternal grandmother (Patient 1C) has posterior embryotoxon, iris hypoplasia, glaucoma and cataract, as well as dental defects and maxillary hypoplasia; no umbilical anomalies are noted. All three affected individuals were found to carry the heterozygous missense mutation c.271C > T, p.(Arg91Trp) in *PITX2*. While this specific mutation has not been reported previously, the mutation is predicted to be damaging by 5/5 in silico prediction packages, and a similar mutation affecting the same codon, c.272G > C, p.(Arg91Pro), has been reported (1). Screening of *FOXC1* identified the benign c.1359_1361dupCGG, p.(Gly456dup) allele in Patient 1A.

Patient 2A is a 46-year-old Caucasian male from Serbia with ARS. He has bilateral posterior embryotoxon, iris processes, glaucoma and maxillary hypoplasia; dental and umbilical findings are unknown. His son, Patient 2B, also has bilateral posterior embryotoxon, iris processes and glaucoma. Non-ocular anomalies include redundant periumbilical skin, maxillary hypoplasia with a broad nasal bridge, and severe mental retardation and seizures thought to be caused by neonatal asphyxiation. No details are available regarding his dental phenotype. Both Patient 2A and his son carry the *PITX2* heterozygous missense mutation c.259T > C, p.(Phe87Leu), similarly predicted to be damaging by 5/5 in silico prediction packages. Screening of *FOXC1* identified both common duplications listed above and the rare in-frame deletion; co-segregation analysis was performed for the rare benign variant and showed it was present in both affected family members.

Patient 3A is a 54-year-old Caucasian female from the United States with ARS. She displayed bilateral posterior embryotoxon, iris processes, iris hypoplasia, as well as glaucoma diagnosed at 25 years of age. Non-ocular anomalies include microdontia and hypodontia with 16 teeth missing (maxillary nos. 1, 2, 6–11, 14, 16; mandibulary nos. 17, 20, 24, 25, 29, 32), redundant umbilical skin, umbilical hernia, and mitral valve

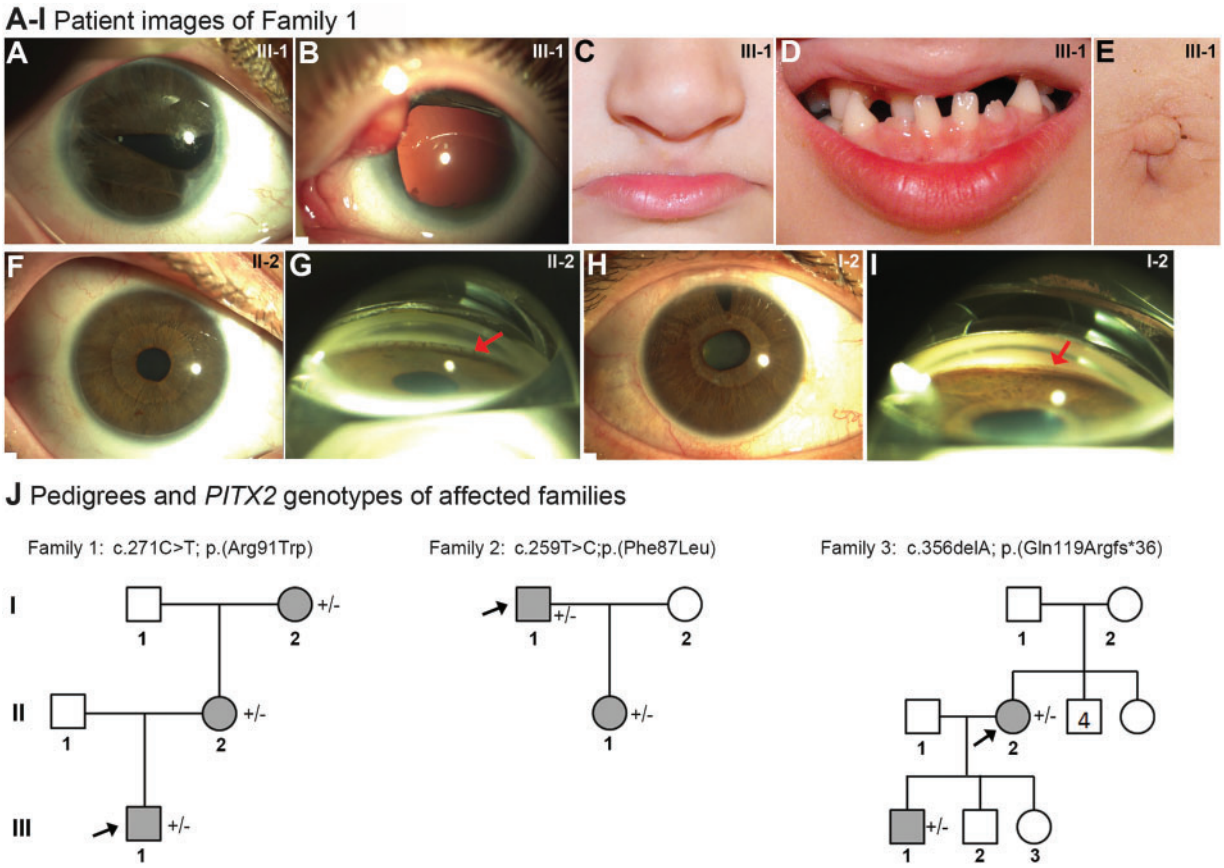

Figure 1. Human patients. Patient images of Family 1. Ocular photos of Patient 1A showing typical features of ARS with corectopia and iris hypoplasia **(A)** in one eye and a more severe phenotype of partial aniridia **(B)** in the other eye. Please also note characteristic systemic features, such as thin upper lip **(C)**, microdontia/hypodontia **(D)**, and mildly redundant periumbilical skin **(E)** in Patient 1A. Ocular photos and goniotomy image from his mother **(F, G)** and grandmother **(H, I)** show iris hypoplasia and iris processes typical of ARS. **(J)** Pedigrees and *PITX2* genotypes of affected families. Gray symbols indicate individuals affected with ARS; + indicates presence of familial mutation; – indicates wild-type *PITX2* allele. Arrow indicates proband.

prolapse. Her son (Patient 3B) is similarly affected with typical ARS ocular features and glaucoma diagnosed at 7 years of age, hypodontia, microdontia, umbilical hernia, Wolf-Parkinson-White syndrome (WPW), and hyperextensibility. Both patients were found to carry the heterozygous frameshift mutation c.356delA, p.(Gln119Argfs*36) in *PITX2*. Screening of *FOXC1* identified the benign c.1139_1141dupGCG, p.(Gly380dup) allele in Patient 3A.

Generation of an allelic series of pitx2 mutations in zebrafish

TALEN-mediated genome editing generated a series of mutations in the region encoding the second α-helix of the *pitx2* homeodomain (Fig. 2). Sequencing of embryos produced by mosaic fish identified five mutant alleles including one premature truncation—c.190_197delATGTCGAC, p.(Met64*); three in-frame deletions—c.193_195delTCG, p.(Ser65del); c.191_196delTGTCGA, p.(Met64_Ser65del); c.191_199delTGTCGACTA, p.(Met64_Thr66del); and one in-frame duplication—c.193_195dupTCG, p.(Ser65dup) (Fig. 2). All mutations were predicted to generate complete or partial loss-of-function alleles due to the disruption of the *pitx2* homeodomain region. Embryos carrying each of the mutant alleles were raised to adulthood, genotyped and crossed to generate homozygous embryos for observation. Four mutant alleles—c.190_197delATGTCGAC, p.(Met64*); c.193_195delTCG, p.(Ser65del); c.191_196delTGTCGA, p.(Met64_Ser65del); and c.193_195dupTCG, p.(Ser65dup)— all produced ~25% of embryos with defects in ocular and craniofacial development. Homozygosity for the corresponding *pitx2* mutations in all abnormal embryos was further confirmed by genotyping; no gross phenotype was detected in heterozygous embryos. Interestingly, the c. 191_199delTGTCGACTA, p.(Met64_Thr66del) line produced a milder, incompletely penetrant phenotype with only 8% of homozygous embryos (2/24 in two distinct crosses) displaying the typical phenotype described above, indicating that this may be a partial loss-of-function (hypomorphic) allele.

The c.190_197delATGTCGAC, p.(Met64*) allele resulting in a premature stop codon and predicted to encode a truncated pitx2 protein lacking the C-terminus and part of the homeodomain (including complete absence of the recognition helix) was selected for further studies and designated *pitx2*^{M64*}. This mutation resembles numerous premature truncation alleles identified in the human *PITX2* gene (Fig. 2), particularly a c.198_201delGTCCinsTTTCT,

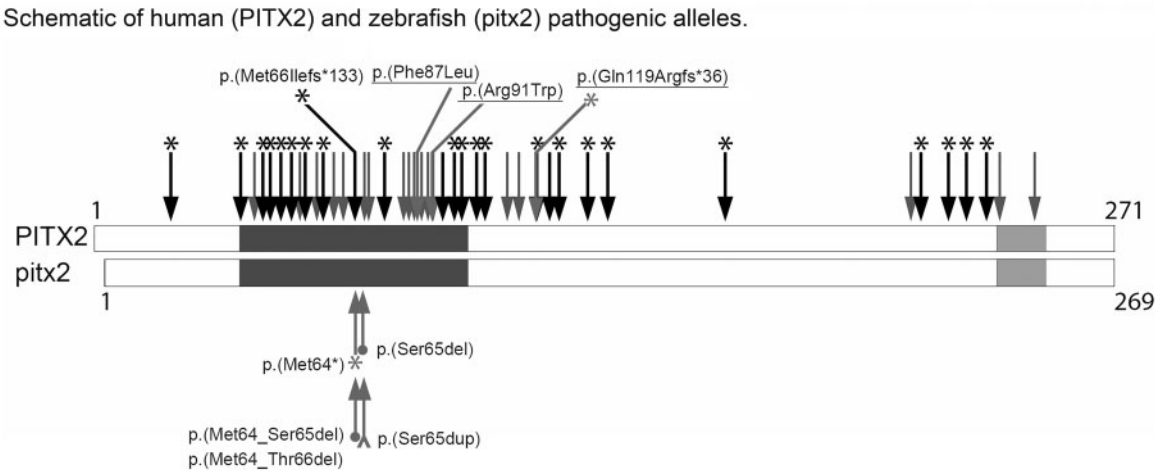

Figure 2. Schematic of human (*PITX2*) and zebrafish (*pitx2*) pathogenic alleles. Human *PITX2* mutations are indicated on the top: black arrows with a star indicate truncating alleles; gray arrows indicate missense alleles. Protein nomenclature is provided for the mutations identified in this study (underlined) as well as the previously reported human mutation most closely resembling the zebrafish alleles generated here. Mutant *pitx2* zebrafish alleles generated by TALEN-mediated genome editing are depicted at the bottom: stars indicate truncating alleles; circles denote in-frame deletion alleles; and carets represent in-frame duplication alleles. Regions corresponding to the homeobox and 14-amino-acid-conserved OAR (Otp, Aristaless, Rx) domains are indicated as dark and light gray boxes, respectively.

p.(Met66Ilefs*133) mutation affecting the same methionine residue within the homeodomain that was identified in ARS (41).

Gross morphological examination of pitx2^{M64*} embryonic and adult phenotypes

Morphological examination revealed that as early as 3-dpf (days post fertilization) the most prominent mutant ocular phenotype was a severely underdeveloped anterior chamber appearing bilaterally in 100% of homozygous *pitx2*^{M64*} embryos (Fig. 3C' and D' versus C and D). Also around this timepoint, ~96% (127 out of 132) of homozygous *pitx2*^{M64*} embryos demonstrated ventral iris colobomas either unilaterally or bilaterally (Fig. 3A' and B' versus A and B). By 5-dpf, in addition to the persistence of the coloboma (Fig. 3E' and F' versus E and F) and underdeveloped anterior chambers, mutant lenses of homozygous *pitx2*^{M64*} embryos appeared elongated in the anterior/posterior plane compared with their spherical wild-type counterparts (Fig. 3G' and H' versus G and H). Craniofacial defects ranging from mild to severe also often accompanied the ocular anomalies. Alcian blue staining of seven 5-dpf mutants and three wild-type siblings showed variable degrees of improper positioning, size and structure of the components of the first (mandibular) and second (hyoid) pharyngeal arches (Fig. 3I versus J–L, M versus N and P).

Homozygous *pitx2*^{M64*} mutants demonstrated reduced survival to adulthood (42 of 404, ~10.5%). Gross ocular phenotypic presentation in those who survived to adulthood ranged from anophthalmia (Fig. 3R) and severe microphthalmia (Fig. 3S) to iris coloboma/hypoplasia (Fig. 3T) and improper globe positioning (Fig. 3U); in some fish, ocular features showed asymmetric presentation (Fig. 3V). Approximately 67% (28 of 42) of mutant adult fish displayed bilateral microphthalmia/anophthalmia (severe), ~21% (9 of 42) showed extremely asymmetric phenotypes with one eye being affected with microphthalmia/anophthalmia/complete globe disorganization and the other eye being grossly normal in size but often misshapen and/or partly opacified (moderate), and ~12% (5 of 42) presented with bilateral normal-sized eyes with subtle shape irregularities and/or opacities (mild). Accompanying craniofacial deformities were also often visible. Incidentally, among homozygous fish surviving to adulthood, only females were capable of successful breeding.

Analysis of ocular phenotype in pitx2^{M64*} mutants by histology and electron microscopy

To characterize the anatomical changes in the *pitx2*^{M64*} homozygous mutant eyes, histological analyses including electron microscopy were performed. These analyses included adult mutants (6) and wild-types (3), 1-mpf (months post-fertilization) mutants (3) and wild-types (3), 14-dpf mutants (3) and wild-types (3) and numerous fish ranging from 3–5 dpf, including 17 mutants and 5 wild-types at 3-dpf. With electron microscopy (performed in 3- and 14-dpf wild-type and mutant embryos), focus was directed primarily on tissues arising from the neural crest, namely the corneal stroma and endothelium, the iris stroma, and the dorsal and ventral iridocorneal angles; development of these structures in zebrafish has been previously described, and our analysis of wild-type specimens corresponded well with the published observations (32). At 3-dpf, early formation of the anterior chamber can be observed as peripheral separation between the cornea and the lens (Fig. 4A). When considering the central cornea, the 3-dpf wild-type eyes display the expected three layers of stratification: epithelium, stroma and endothelium (Fig. 4B–D); because the anterior chamber is early in its development and has not yet fully formed, the central corneal endothelium is found flush against the lens capsule and epithelium (Fig. 4A, B and D). The corneal epithelium is delineated into surface and subepithelial cells which are further distinguished by the presence of many dark-staining small inclusion bodies versus fewer larger inclusion bodies, respectively (Fig. 4B and C). The wild-type corneal stroma is of uniform thickness and on its basal side borders the corneal endothelium (Fig. 4D). In contrast, the 3-dpf *pitx2*^{M64*} mutant does not display distinct lens and cornea separation (Fig. 4A'). The *pitx2*^{M64*} mutant corneal epithelium contains smaller inclusion bodies than wild-type (in both surface and subepithelial layers) and instead exhibits small vacuoles in the surface layer (Fig. 4B' and C'; Supplementary Material, Fig. S2). To the best of our knowledge,

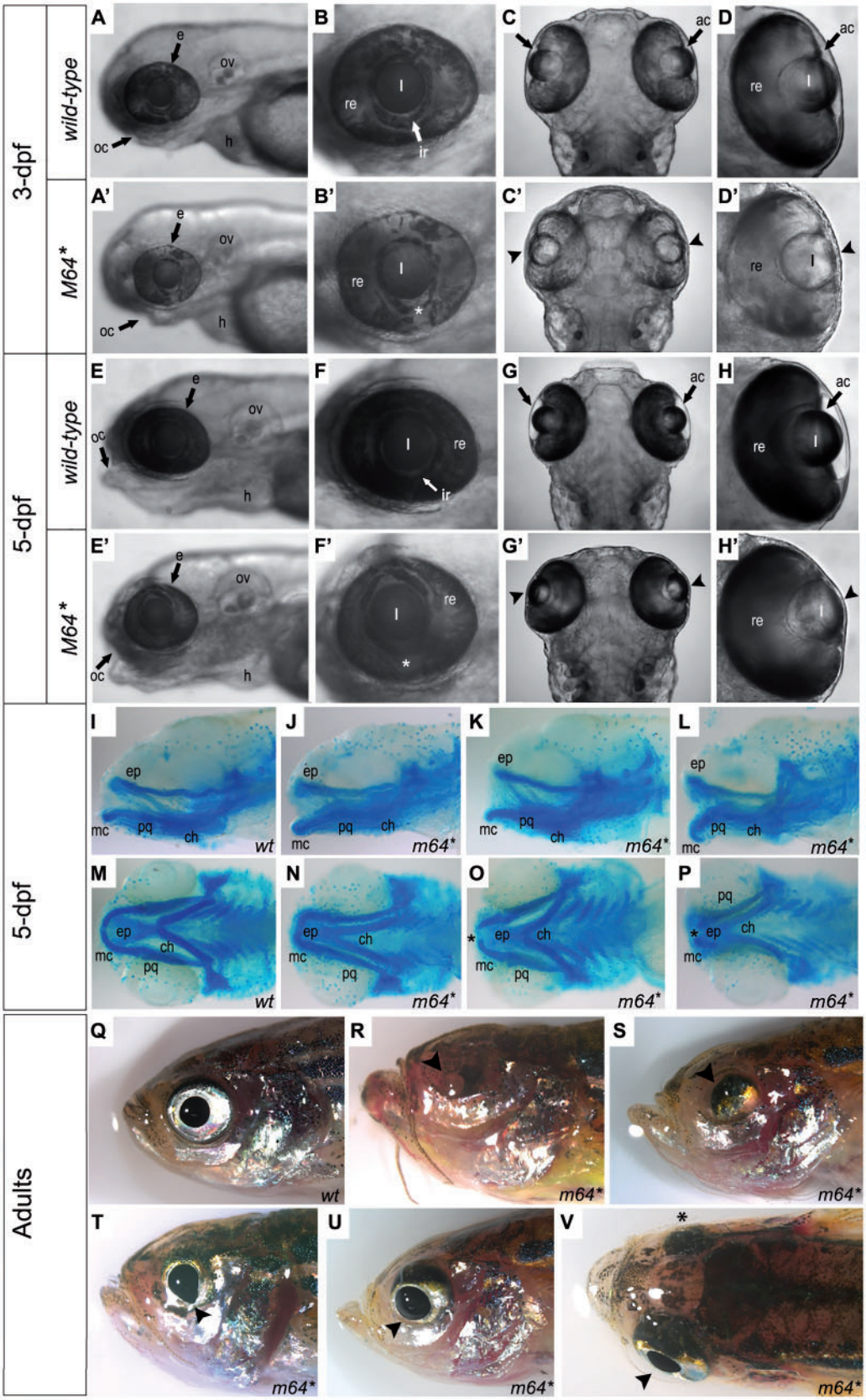

Figure 3. Gross characterization of the *pitx2*^{M64*} mutant phenotype. **(A–H')** Wild-type (A–H) and *pitx2*^{M64*} mutant (A'–H') embryos. At 3-dpf, prominent features include ventral iris coloboma (white asterisk in B' versus B) and bilateral severely underdeveloped ocular anterior chambers (arrowheads in C', D' versus C, D). By 5-dpf, in addition to the persistence of the coloboma (white asterisks in F' versus F) and underdeveloped anterior chambers (arrowheads in G', H' versus G, H), mutant lenses of

the significance of the inclusion bodies in the corneal epithelium of zebrafish embryos has not yet been determined. The mutant corneal stroma appears thicker in some places and less uniform than its wild-type counterpart; however, the difference is not significant. In addition, the mutant appears to lack a defined corneal endothelium and lens capsule, as the corneal stroma sits directly adjacent to the lens epithelial cells (Fig. 4D').

In terms of the iridocorneal region, at 3-dpf the periocular mesenchymal cells of wild-types have begun their differentiation into iris stroma, consisting of pigment cells—namely xanthophores and iridophores—as well as embryonic vasculature and non-pigment cells (Fig. 4E–H). The iris pigmented epithelium has developed from the retinal neuroepithelium and is producing characteristic black melanosomes (Fig. 4E–H). In contrast, the iridocorneal angles of 3-dpf *pitx2*^{M64*} homozygous mutants exhibit numerous structural differences from their wild-type counterparts. The composition of the anterior chamber fluid-filled space in *pitx2*^{M64*} eyes is marked by an excess of cellular material (Fig. 4E'–H'). Possible sources of this material include aberrant lipid or protein secretion, cellular sloughing/degradation or undifferentiated cells which could be attributed to the notable under-differentiation of the iris stroma. While the dorsal iris stroma presents some evidence of delayed pigment differentiation and organization (Fig. 4E'–F'), the ventral angle displays a complete lack of iris stroma differentiation (Fig. 4G'–H'). In addition, though ventral iris pigmentation is generally delayed compared with dorsal pigmentation, the *pitx2*^{M64*} mutant ventral angle shows a pronounced absence of melanosomes in the most anterior portion of the iris pigmented epithelium at this timepoint (Fig. 4G'–H').

Examination of 14-dpf wild-type and *pitx2*^{M64*} mutant embryos reveals persistence of the defects observed at the earlier stage (Fig. 5A versus A'). With respect to the cornea, the 14-dpf wild-type cornea is clearly stratified into its three components: a three- to four-cell layer thick epithelium; a smooth, even-thickness stroma; and a uniform single layer endothelium (Fig. 5B–D). The corneal endothelium is distinctly separated from the lens capsule and epithelium by the anterior chamber space filled with a proteinous liquid (aqueous humor) (Fig. 5B). The most noteworthy observation upon inspection of the 14-dpf *pitx2*^{M64*} mutant eyes is the absence of the anterior chamber space, which places the mutant cornea directly up against the lens capsule (Fig. 5A'–D'). The 14-dpf *pitx2*^{M64*} mutant cornea seems to have three layers; however, the innermost layer of subepithelium, stroma, and endothelium appear wavy and of fluctuating thickness (Fig. 5B'–D'). The presumptive corneal endothelium in particular is contoured between the stroma and lens capsule; before additional staining (see below), it was difficult to say whether the observed layer is in fact a monolayer endothelium or the compressed remnants of the anterior chamber space (Fig. 5C'–D').

At 14-dpf, the anterior chamber is more developed and manifests as a defined space between the lens and cornea with separation between the iris and lens and no occlusion of the iridocorneal angles (Fig. 5A, E and H–J). Iridocorneal angles of 14-dpf wild-type eyes show further differentiation of the iris stroma as well as the presumptive annular ligament (Fig. 5E, G, I and K). In the dorsal angle, ciliary zone non-pigmented epithelial cells have begun to anteriorly differentiate into secretory cells (Fig. 5E and F). These cells are the source of aqueous humor production in zebrafish and will continue to develop a more secretory appearance (32,36). In the ventral angle, differences in specialization instead form structures specific for aqueous humor drainage. A canalicular drainage network consisting of two main branches arises over the first month of development; the iridocorneal canal presents as a channel within a non-pigmented mesothelial layer separating the annular ligament from the iris stroma, and the ciliary canal appears as an endothelium-lined passage through the pigmented epithelial base of the iris (32,36). In the ventral angle, formation of both channels of the canalicular drainage network can be observed by 14-dpf (Fig. 5I, K and L). Examination of the 14-dpf *pitx2*^{M64*} mutant shows a notable reduction of the anterior chamber space between the cornea and the lens as well as at both iridocorneal angles, with the iris pigmented epithelium remaining markedly in contact with the lens (Fig. 5A', E', H', I' and J'). The iris stroma and presumptive annular ligament appear delayed in their differentiation (Fig. 5E', G', I', K' and L'). In addition, the dorsal non-pigmented ciliary epithelium does not appear to have begun differentiation, as the cells immediately adjacent to the iris pigmented epithelium maintain their retinal neuroepithelial morphology (Fig. 5E' and F'). In the ventral angle, the only indication of specialization is the break in the iris pigmented epithelium marking the presumptive location of the ciliary canal (Figure 5I' and K'); aside from this, the endothelial lining of the canal has failed to differentiate, and the iridocorneal drainage canal is undetectable (Fig. 5I', K' and L').

Histological sectioning of six mutant and three wild-type adult fish revealed a spectrum of gross phenotypes (Fig. 6A–C). The most prevalent phenotype includes the absence of both the anterior and posterior chambers as well as a severe reduction or complete absence of the iris (Fig. 6B and C). In the corneal region, drastic structural differences are observed in comparison to the wild-type counterpart. The adult wild-type corneal epithelium contains four to six layers of nonkeratinized, stratified squamous cells (33) as observed in our controls (Fig. 6D). In the mutant fish, the epithelium is thicker, and a subset of cells takes on a larger columnar morphology closely resembling that of the epidermal stratified epithelium surrounding the head (Fig. 6E and F). The corneal stroma of the wild-type is of uniform thickness, whereas the equivalent mutant layer is generally thinner, wavier in appearance, and sometimes interrupted (Fig. 6D and E). In place of the single-layer wild-type corneal endothelium, the analogous region in the mutant is a noticeably thickened, disorganized layer of cells of unknown origin (Fig. 6D–F). Aberrant pigmentation is also typically observed in the mutant corneal epithelium and endothelium (Fig. 6E–F). In addition, some of the eyes that appeared opaque or hidden by gross analysis were found to be covered by skin and cartilage structures growing together over the eye globe (Fig. 6B, C, E and F).

homozygous *pitx2*^{M64*} embryos appear elongated in the anterior/posterior plane (G', H' versus G–H). Craniofacial abnormalities also become apparent in mutants (E' versus E). Views are lateral (A, B, A', B', E, F, E', F') and dorsal (C, D, C', D', G, H, G', H'). **(I–P)** Alcian blue staining of 5-dpf wild-type (I, M) and *pitx2*^{M64*} mutant (J–L, N–P) embryos. A range of mild to severe structural malformations were evident in the Meckel's cartilage, mc, palatoquadrate, pq, (first pharyngeal arch) and ceratohyal, ch, (second pharyngeal arch) (I versus J–L, M versus N–P). Views are lateral (I–L) and ventral (M-P). **(Q–V)** Wild-type (Q) and *pitx2*^{M64*} mutant (R–V) adult fish. Gross ocular phenotypic presentation included anophthalmia (R), microphthalmia (S), and enlarged/misshapen pupils with improper globe orientation (T, U) and could appear asymmetrically (as in V; arrowhead versus asterisk). Views are lateral (Q–U) and dorsal (V). ac, anterior chamber; e, eye; h, heart; ir, iris; l, lens; oc, oral cavity; ov, otic vesicle; re, retina; ep, ethmoid plate; mc, Meckel's cartilage (P1); pq, palatoquadrate (P1); ch, ceratohyal (P2); hs, hyosympletic (P2).

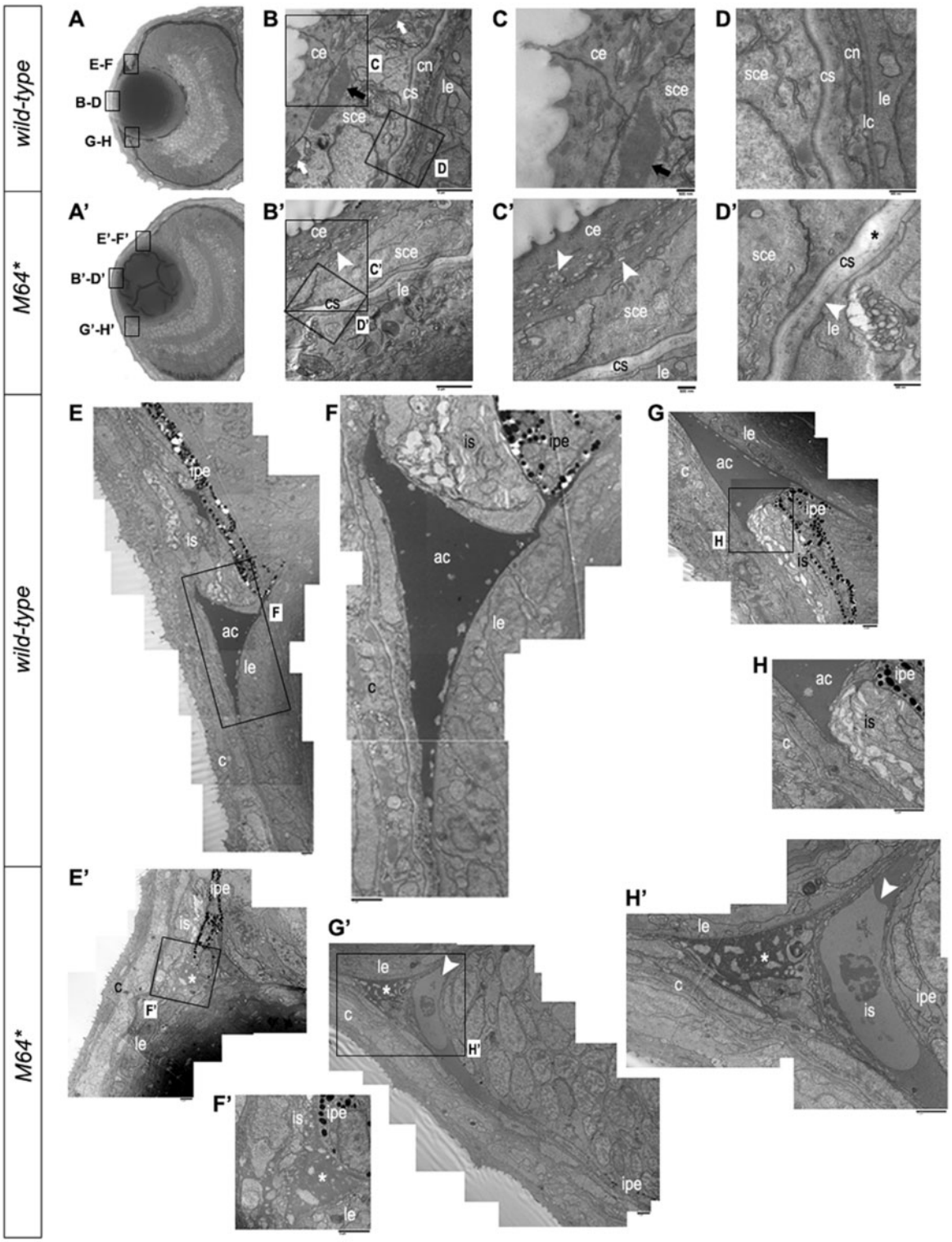

Figure 4. Electron microscopy of 3-dpf anterior chamber structures. **(A, A')** Histological sections depicting orientation of wild-type (A) and *pitx2*^{M64*} mutant (A') eyes. **(B–D, B'–D')** Wild-type (B–D) and *pitx2*^{M64*} mutant (B'–D') central corneas. Wild-type eyes display three layers of stratification: epithelium, stroma and endothelium (B). The corneal epithelium is delineated into surface and subepithelial cells distinguished by many dark-staining small inclusion bodies versus fewer larger inclusion bodies, respectively (arrows in B, C). The wild-type corneal stroma is of uniform thickness and on its basal side borders the corneal endothelium (D). In contrast, corneal defects in the mutants include an epithelium that contains smaller inclusion bodies in both layers and exhibits small vacuoles in the surface layer (arrowheads in B', C'), a thicker and uneven stroma (asterisk in D'), and lack of a defined endothelial layer (arrowhead in D'). **(E–H')** Wild-type (E–H) and *pitx2*^{M64*} mutant (E'–H') iridocorneal angles. Dorsal (E–F) and ventral (G–H) angles displayed early formation of the anterior chamber space as well as early differentiation of the iris stroma and iris pigmented epithelium. In mutants, both dorsal (E', F') and ventral (arrowheads in G', H') iridocorneal angles display notable under-differentiation of the iris stroma and iris pigmented epithelium, particularly ventrally; in addition, the anterior chamber space is marked by an excess of cellular material (asterisks in E', H'). ce, corneal epithelium; cn, corneal endothelium; cs, corneal stroma; lc, lens capsule; le, lens epithelium; sce, corneal subepithelium; ac, anterior chamber; c, cornea; is, iris stroma; ipe, iris pigmented epithelium.

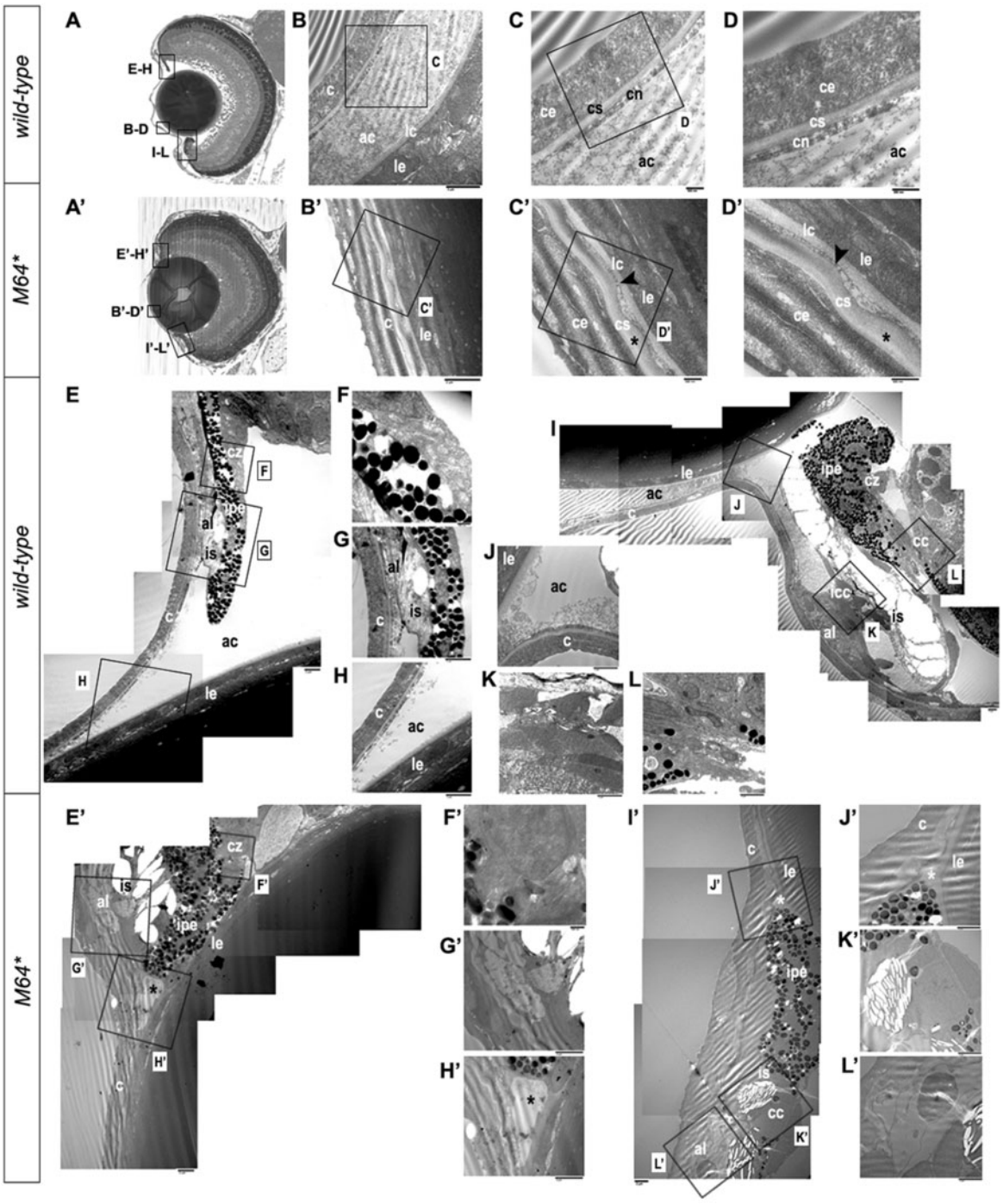

Figure 5. Electron microscopy of 14-dpf anterior chamber structures. Histological sections depicting orientation of wild-type **(A)** and *pitx2*^{M64*} mutant **(A')** eyes. Wild-type **(B–D)** and *pitx2*^{M64*} mutant **(B'–D')** central corneas. The wild-type cornea is clearly stratified into its three component layers: a three- to four-cell layer thick epithelium; a smooth, even-thickness stroma; and a uniform single layer endothelium (B–D). The corneal endothelium is distinctly separated from the lens capsule and epithelium by the anterior chamber space (B). In mutants, the anterior chamber space is absent, placing the mutant cornea directly up against the lens capsule (B'–D'). The innermost layer of subepithelium and stroma appear wavy and of fluctuating thickness (asterisks in C', D'). The presumptive corneal endothelium, be it a monolayer endothelium or the compressed remnants of the anterior chamber space, is contoured between the stroma and lens capsule (arrowheads in C', D'). Wild-type **(E–L)** and *pitx2*^{M64*} mutant **(E'–L')** iridocorneal angles. Wild-type dorsal (E–H) and ventral (I–L) angles display a distinct anterior chamber space with separation between lens and cornea and no angle occlusion (E, H–J); in addition, further differentiation of the iris stroma and the presumptive annular ligament is also demonstrated (E, G, I, K). Dorsally, the ciliary zone non-pigmented epithelial cells have begun to anteriorly differentiate from the retinal neuroepithelium (E, F). Ventrally, the formation of the iridocorneal canal and the ciliary canal, the two main branches of the specialized canalicular drainage network, can be observed (I, K, L). In contrast, the mutant shows a notable reduction in the anterior chamber space at both iridocorneal angles, with the iris pigmented epithelium remaining markedly in contact with the lens (asterisks in E', H'–J'). The iris stroma and presumptive annular ligament appear delayed in their differentiation (E', G', I', K', L'). Dorsally, the non-pigmented ciliary epithelium does not appear to have begun differentiation (E', F'). Ventrally, the only indication of specialization is the break in the iris pigmented epithelium marking the presumptive location of the ciliary canal (I', K'); aside from this, the endothelial lining of the canal has failed to differentiate, and the iridocorneal drainage canal is undetectable (I', K', L'). ac, anterior chamber; c, cornea; ce, corneal epithelium; cn, corneal endothelium; cs, corneal stroma; lc, lens capsule; le, lens epithelium; al, annular ligament; cc, ciliary canal; cz, ciliary zone; icc, iridocorneal canal; ipe, iris pigmented epithelium; is, iris stroma.

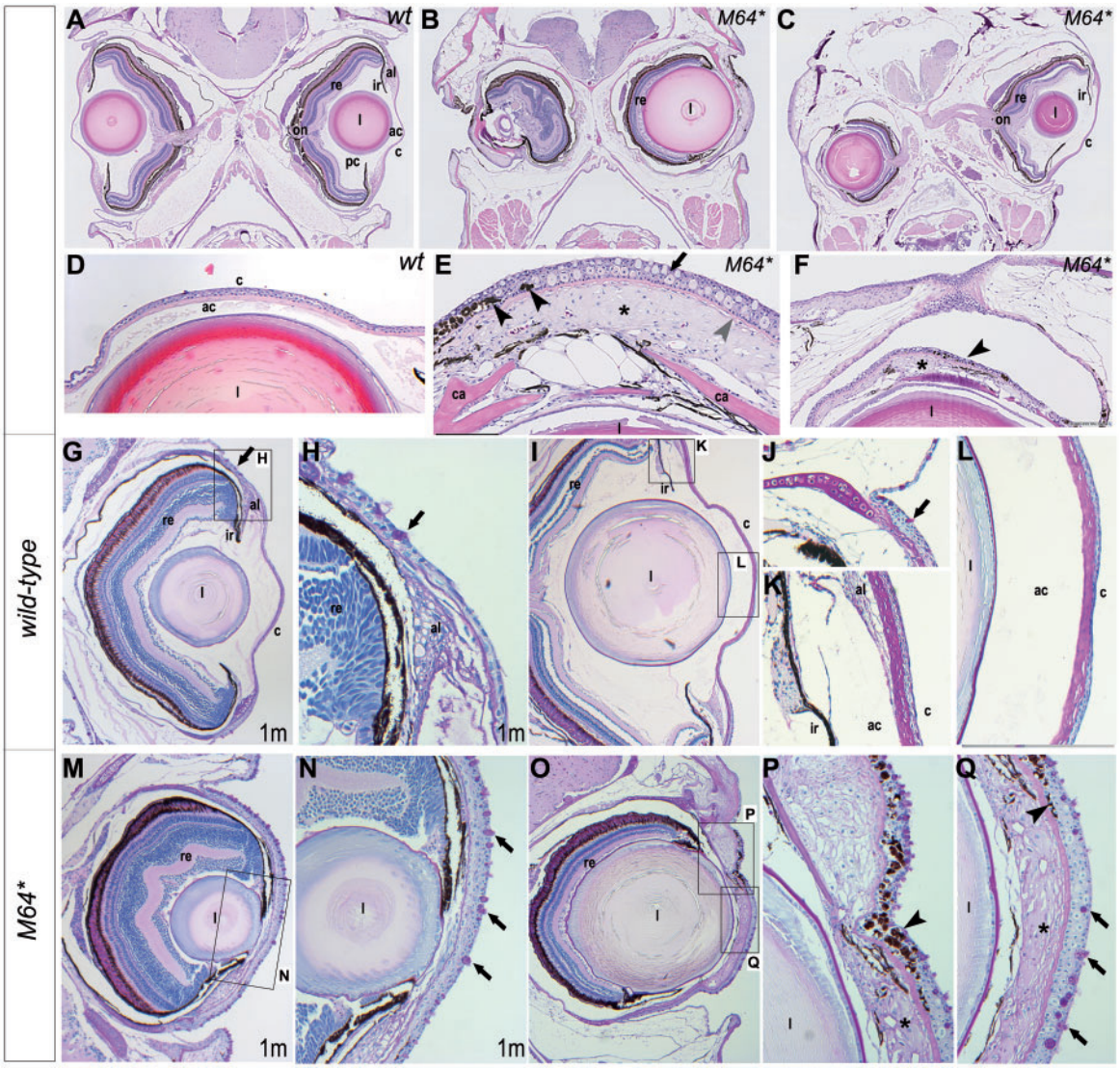

Figure 6. Histological analysis of adult *pitx2*^{M64*} mutant phenotype. H&E transverse sections of wild-type **(A, D)** and *pitx2*^{M64*} mutant **(B, C, E, F)** heads and corneas. Gross mutant phenotypes range from mild thickening of the corneal epithelium (C) to complete disorganization of the entire optic globe (B). The most prevalent phenotype includes the absence of both the anterior and posterior chambers as well as a severe reduction or a complete absence of the iris (B, C). In the cornea, the wild-type displays a typical stratified squamous epithelium, a uniformly thick stroma, and a single-layer endothelium (D). Mutant corneal epithelium is thicker, and a subset of cells takes on larger columnar morphology resembling that of epidermal stratified epithelium (black arrow in E). Mutant corneal stroma appears thinner, wavier, and sometimes interrupted (gray arrowhead in E). The analogous monolayer corneal endothelium region in the mutant is a noticeably thickened, disorganized layer of cells of unknown origin (black asterisk in E, F). Aberrant pigmentation is also typically observed in the mutant corneal epithelium and endothelium (black arrowheads in E, F), as well as cartilaginous layers (ca) in the anterior segment of mutant eyes (E, F). Some eyes that appeared opaque or hidden by gross analysis were found to be covered by skin and cartilage structures growing together over the eye globe (B, C, E, F). PAS staining of 1-mpf **(G, H, M, N)** and adult **(I–L, O–Q)** transverse sections. In wild-type adults 1-mpf and older, mucin-secreting goblet cells are present in the eye periphery (black arrows in G, H, J) but absent from the central corneal epithelium (G–I, K, L). In contrast, age-matched mutants develop goblet cells throughout the entire corneal epithelium (M–Q; black arrows in N and Q). Aberrant pigment deposits (black arrowheads in P, Q) and disorganized tissue next to the lens (asterisks in P, Q) are also evident. ac, anterior chamber; al, annular ligament; c, cornea; ca, cartilage; ir, iris; l, lens; re, retina; on, optic nerve; pc, posterior chamber.

Taken together, this data suggests that complete deficiency in *pitx2* results in abnormal development of the cornea, iris, and iridocorneal region and leads to severe ocular disorganization in adult fish.

Analysis of pitx2^{M64*} mutants with various markers

To further examine the observed ocular phenotype in *pitx2*^{M64*} homozygous mutants, additional analysis with various markers was performed. Periodic Acid Schiff staining (PAS) was used to visualize mucin-secreting goblet cells in the conjunctiva and other epithelium (21). N-cadherin (cdh2), which marks the corneal endothelium (29) as well as both the corneal and lens epitheliums in zebrafish (42) was also employed. To visualize the corneal stroma, collagen1a1a (col1a1a), a member of the collagen 1 family which is a key component of stromal collagen fibrils, and corneal keratan sulfate proteoglycan (CKS) were utilized (33,43).

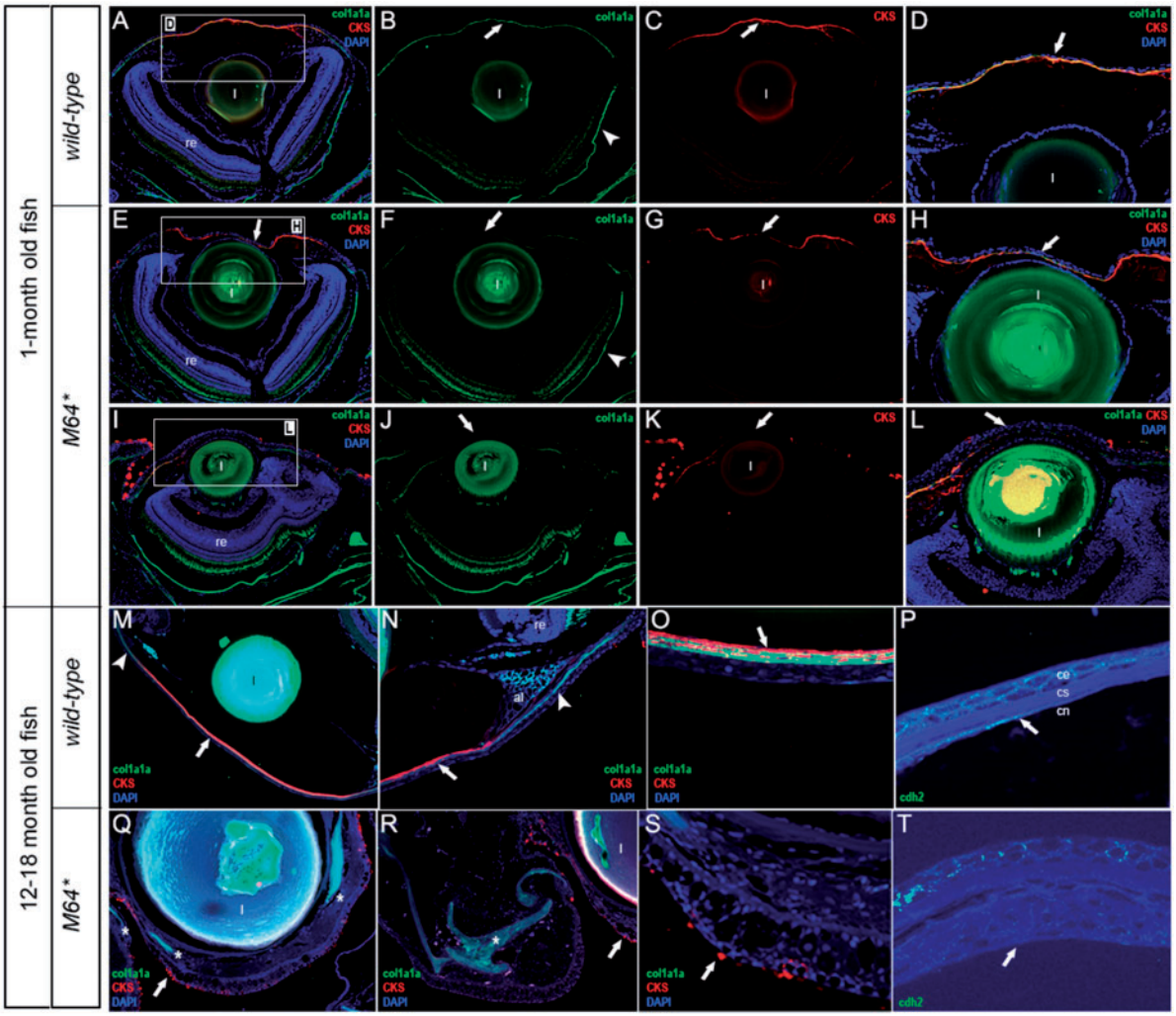

Figure 7. Immunohistochemical analysis of 1-mpf and adult *pitx2*^{M64*} mutant phenotype. 1-mpf wild-type (**A–D**) and *pitx2*^{M64*} mutant (**E–L**) sections stained with col1a1a (green), CKS (red) and DAPI (blue). D, H and L represent magnified images of the corresponding boxed regions in A, E and I. Wild-type corneal stroma staining reveals a continuous, uniform stromal layer with col1a1a (A, B, D) appearing both in the cornea (arrows in B and D) and around the eye (arrowhead in B) and CKS (A, C, D) being specific to the corneal stroma (arrows in C, D). In mutants, interruptions in or absence of col1a1a (E, F, H–J, L) and CKS (E, G–I, K, L) staining indicates disorganization of the corneal stroma (arrows in E–H, J–L). CKS also detects mucin-secreting goblet cells in the eye periphery and aberrantly approaching the corneal epithelium (I, K, L). Adult wild-type (**M–O**) and *pitx2*^{M64*} mutant (**Q–S**) sections stained with col1a1a (green), CKS (red) and DAPI (blue). Wild-type adult corneal stroma continues to co-express col1a1a and CKS in a continuous layer (arrows in M and O) with CKS localized specifically to the cornea (arrows in M, N) and col1a1a also present around the eye (arrowheads in M, N). In mutant adults, col1a1a and CKS staining is absent from the corneal stroma region (Q). Instead, col1a1a stains ectopic cartilage structures in the endothelial region and ocular periphery (asterisks in Q, R,), whereas CKS stains mucin-secreting goblet cells in both the eye periphery and corneal epithelium (arrows in Q–S). Adult wild-type **(P)** and *pitx2*^{M64*} mutant **(T)** sections stained with N-cadherin (green). In wild-type corneas, cdh2 detects both the corneal epithelium and the monolayer corneal endothelium (arrow in P). In mutants, while cdh2 staining was detectable but less robust in the epithelium, it did not appear in the endothelial region indicating the absence of a defined corneal endothelial layer (arrow in T). al, annular ligament; ce, corneal epithelium; cn, corneal endothelium; cs, corneal stroma; l, lens, re, retina.

PAS staining demonstrated that in wild-type 1-mpf and older fish, mucin-secreting goblet cells are present in the eye periphery (Fig. 6G, H and J) but absent from the central corneal epithelium (Fig. 6G–I, K and L). However, goblet cells are detected throughout the entire corneal epithelium in age-matched *pitx2*^{M64*} homozygous mutants, suggestive of a shift from corneal epithelial identity to an epidermis-like layer (Fig. 6M–Q).

Immunostaining of 1-mpf wild-type corneal stroma staining reveals a continuous, uniform stromal layer, with col1a1a appearing both in the cornea and around the eye (Fig. 7A, B and D) and CKS being specific to the corneal stroma (Fig. 7A, C and D). In *pitx2*^{M64*} homozygous mutants, interruptions in or absence of col1a1a (Fig. 7E, F, H–J and L) and CKS (Fig. 7E, G–I, K and L) staining indicates disorganization of the corneal stroma. CKS also detects mucin-secreting goblet cells in the eye periphery and aberrantly approaching the corneal epithelium in mutant eyes (Fig. 7I, K and L). Wild-type adult corneal stroma continues to co-express col1a1a and CKS in a continuous layer (Fig. 7M and O) with CKS localized specifically to the cornea (Fig. 7M–O). In mutant adults, col1a1a and CKS staining is absent from the corneal stroma region (Fig. 7Q). Instead, col1a1a stains ectopic cartilage structures in the endothelial region and ocular periphery (Fig. 7Q–R), whereas CKS stains mucin-secreting goblet cells in both the eye periphery and corneal epithelium (Fig. 7Q–S).

Immunostaining with n-cadherin (cdh2) in wild-type corneas detected both the corneal epithelium and the monolayer corneal endothelium (Fig. 7P). In mutants, while cdh2 staining was detectable but less robust in the epithelium, it did not appear in the endothelial region, indicating the absence of a defined corneal endothelial layer (Fig. 7T). Thus, the unusual corneal region bears a striking morphological resemblance to the skin and connective tissue structures of the surrounding head, suggestive of a possible loss of corneal cell fate or a fate switch to epidermal skin at some point during development.

To identify the initial processes affected in *pitx2* mutants that lead to the abnormal eye development, we analyzed migration patterns and cell death during the early steps of eye development. The migration of *pitx2*-positive periocular mesenchyme was assessed using *in situ* hybridization (ISH) with *pitx2*- and *foxc1*a-specific probes in wild-type and mutant embryos. The abnormal *pitx2* transcript expressed in homozygous *pitx2*^{M64*} mutants was detectable at comparable to wild-type levels, suggesting that the mutant transcript is not subject to nonsense mediated decay. Staining with a probe recognizing both *pitx2* isoforms performed in 48-hpf (hours post fertilization) embryos revealed no obvious differences in the distribution of abnormal *pitx2* transcript in homozygous mutant embryos in comparison to normal *pitx2* in wild-type fish. Staining for the *foxc1a* transcript, another marker of anterior segment development, similarly identified no obvious differences between *pitx2*^{M64*} homozygous and control embryos (Supplementary Material, Fig. S1). This data suggests no obvious defects in migration of neural crest cells expressing mutant *pitx2* to their proper locations within the developing eye.

Terminal deoxynucleotidyl transferase dUTP nick end labeling (TUNEL) staining to visualize possible aberrant increases in apoptotic cell death indicated that 48–120-hpf control embryos (with at least 10 embryos per stage) display few to no apoptotic cells in the cornea-lens region. The *pitx2*^{M64*} homozygous mutant embryos at the same stages [48-hpf (16), 72-hpf (12), 96-hpf (5) and 120-hpf (8)] did not show a consistent increase in TUNEL staining overall but tended to have more apoptotic cells in the lens-cornea region, either as individual puncta or larger patches of stained cells at variable locations (Supplementary Material, Fig. S1); in addition to affecting only a subset of mutant fish, the observations were often unilateral. Though these experiments suggested an increase in apoptosis in some *pitx2* mutants, the noted effects do not seem to be sufficient to explain the observed ocular abnormalities which, together with generally normal migration pattern, suggests that *pitx2* function is required for proper differentiation of the cornea, iris and iridocorneal tissues.

Identification of downstream pathways affected in pitx2^{M64*} embryonic tissues via global transcriptome analysis

To begin to ascertain the downstream pathways that are disrupted in *pitx2*^{M64*} homozygous mutants, RNA from 23-hpf wild-type and *pitx2*^{M64*} homozygous eyes only was submitted for microarray analysis. The *pitx2*^{M64*} mutants show no visible phenotype at 23–24-hpf, with *pitx2*-positive periocular mesenchymal cells surrounding the eye and completing their migration to the anterior segment region for subsequent differentiation. With this, the possible transcriptome changes detected at this developmental stage are expected to be due to deficiency in activating/repressing early pitx2 targets as well as their likely secondary effects rather than the result of the structural ocular abnormalities seen at later stages. The resulting list of differentially expressed genes identified 2226 down-regulated and 2044 up-regulated transcripts in *pitx2*^{M64*} homozygous mutants as compared with wild-type controls. Full microarray data are available in the ArrayExpress database at EMBL-EBI (www.ebi.ac.uk/arrayexpress) under accession number E-MTAB-6463.

The analysis was further focused on genes that demonstrated a significant decrease (2-fold or higher) in their expression, based on previous characterization of PITX2 as an activator (44). Pathway analysis of these significantly downregulated transcripts using Ingenuity Pathway Analysis identified enrichment of several broad categories including cell movement, head development, and eye formation and morphology (Supplementary Material, Table S2), as well as signaling pathways, such as Wnt/β-catenin, PCP, calcium, actin cytoskeleton, Rho GTPase, epidermal growth factor (EGF), platelet-derived growth factor platelet-derived growth factor (PDGF) and integrin signaling. In several of these lists, the presence of multiple members of the WNT signaling pathway as well as collagen gene transcripts was notable. Analysis of the entire list of significantly (x2 or more) downregulated targets identified six WNT transcripts— *wnt3, wnt4a, wnt6b, wnt7aa, wnt9b* and *wnt10a*, as well as multiple transcripts of *tert* encoding a transcriptional modulator of WNT/beta-catenin signaling (45), and seven collagen transcripts, *col1a1a, col1a2, col5a2b, col5a3b, col7a1*, *col12a1* and *col14a1*, with orthologs present in humans. Further analysis of these genes using publicly available resources (http://biogps.org; https://www.ncbi.nlm.nih.gov/pubmed/) revealed their expression in mouse ocular structures, with an enrichment in iris, cornea, eyecup and ciliary bodies similar to *Pitx2* (Supplementary Material, Fig. S3), as well as possible roles in anterior segment phenotypes (46–52). Genes associated with the strongest expression/possible function in anterior segment structures, including all identified WNT transcripts and four collagens, *col1a1a, col1a2, col5a2b* and *col5a3b*, were selected for further investigation (Fig. 8 and Table 2). RNA transcript analysis by qPCR confirmed that all 11 selected targets were reduced at 24-hpf, as predicted by the microarray (Fig. 8). Apart from *col5a2b* and *wnt7aa*, the other nine targets were also persistent in their downregulation through 48- and 72-hpf, corresponding to the onset of the *pitx2*^{M64*} homozygous phenotype (Fig. 8).

Discussion

Patients with *PITX2* mutations usually display ARS with typical ocular anomalies (posterior embryotoxon, iris hypoplasia and/or iris processes, pupillary anomalies) and other systemic features (most commonly dental and umbilical defects). More rarely reported ocular phenotypes include various corneal anomalies, such as Peters anomaly (characterized by corneal opacity, defects in the posterior layers of the cornea, iris processes and/or corneolenticular adhesions), ring dermoid of the cornea (diagnosed based on the presence of limbal dermoids at the cornea/conjunctival border), or microcornea (a small corneal diameter) (2,3). Many ARS patients (~50%) develop an increased, and poorly manageable, IOP that leads to optic nerve damage and visual impairment; since the iridocorneal angle appears to be mostly open in ARS patients, the increased IOP is believed to

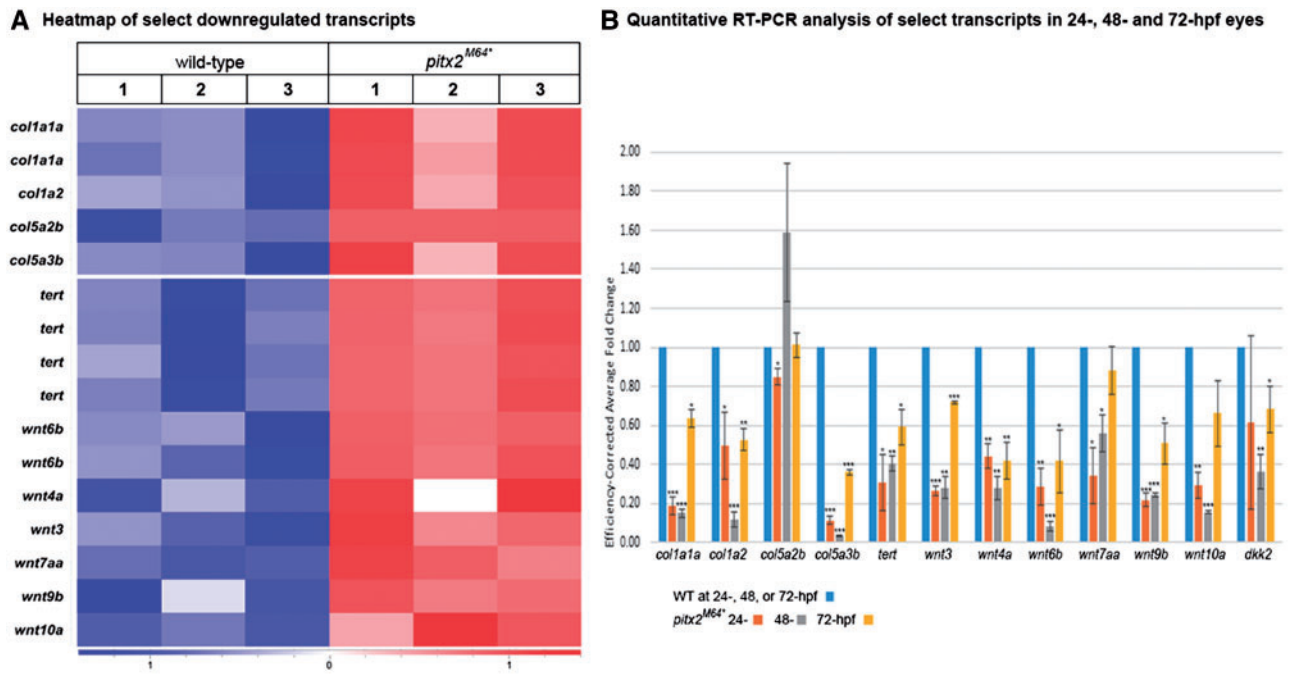

Figure 8. Microarray target analysis. **(A)** Heatmap of selected transcripts identified by microarray as potential downstream targets of pitx2. **(B)** Down-regulation of eleven selected transcripts was independently confirmed by quantitative RT-PCR at 24, 48 and 72-hpf. *dkk2*, a previously reported downstream target of Pitx2 during mouse eye development (21), was included for comparison. Statistical significance is indicated by asterisks (compared with wild-type values) as follows: a single asterisk corresponds to $P < 0.05$; two asterisks to $P < 0.01$; three asterisks to $P < 0.001$.

be associated with incomplete formation of the trabecular lamellae and Schlemm's canal (53).

The patients presented in this article demonstrated typical features of ARS along with some additional less frequent findings. One individual in Family 1 was reported to have corneal guttata; a literature search identified a few additional cases of ARS with corneal guttata/Fuch's dystrophy with confirmed *PITX2* mutations in two families (54–56). Corneal guttata affects the corneal endothelium and is part of Fuch's dystrophy, which is characterized by the formation of lesions between the corneal endothelium and Descemet's membrane resulting in death of the endothelial cells. Another patient in Family 3 was diagnosed with WPW. Some people with WPW display atrial fibrillation, which has been independently associated with alterations in *PITX2* expression in patients without ARS (57). Other unusual features present in our patients included severe mental retardation and seizures observed in Patient 2B (though possibly related to neonatal asphyxiation) and mitral valve prolapse and hyperextensibility also seen in Family 3.

To gain insight into the mechanisms of *PITX2*-associated phenotypes, we generated mutations in zebrafish *pitx2* that are expected to result in a complete knockout. The *pitx2*^{M64*} mutant line was selected for further studies. The zebrafish p.(Met64*) allele most closely resembles the human p.(Met66Ilefs*133) mutation that was identified in an ARS family with typical eye, craniofacial and dental features (no umbilical anomalies noted); one family member demonstrated a more severe ocular presentation with corneal edema, sclerocornea, and pigment deposition on the nasal and temporal peripheral corneal endothelium (41). The zebrafish *pitx2*^{M64*} mutants exhibited related ocular and craniofacial defects. Ocular anomalies included all three layers of the cornea: absence of an identifiable corneal endothelium as early as 3-dpf and persisting through adulthood; disruption or absence of the stroma; and an apparent fate shift from corneal epithelium to head epidermis, complete with aberrant pigmentation and ectopic collagenous structures. In addition, from early embryonic stages the development of the iris, iridocorneal angles, and ciliary zone are significantly disrupted such that these structures are extremely reduced, lack proper differentiation, or are absent in most *pitx2* mutant adult eyes. With respect to craniofacial development, *pitx2* mutants display structural and positional malformations of the first and second pharyngeal arches.

Several findings observed in *pitx2*^{M64*} fish deserve special attention. The first is the progressive loss of corneal identity, with the corneal epithelium taking on an epidermal-like fate. A similar phenotype has been previously reported in mice with temporal *Pitx2* ablation that demonstrated a shift in gene/protein expression profiles of their developing corneas to more closely resemble conjunctival tissue (58). A suggested mechanism involves interaction with the WNT pathway. Mice with deficiency of *Dkk2* (an extracellular antagonist of canonical Wnt-β-catenin signaling and a previously identified downstream target of Pitx2) show corneal abnormalities, including a complete fate shift from corneal epithelium to stratified epidermis in some animals; the shift is attributed to aberrant regulation of localized Wnt signaling throughout the ocular mesenchyme and limbus (21,59). In humans, one report connected a missense mutation in *PITX2*, p.(Arg62His), with ring dermoid of the cornea [MIM180550] in a large Chinese pedigree (12,60,61). Genetic studies in other human pedigrees affected with corneal dermoid and related phenotypes (62) may provide additional information about possible other *PITX2* mutations in these conditions. Also, the data presented in this manuscript provide further support for the interaction between PITX2 and the WNT pathway and encourage further investigation into their relationship (see below).

Another relevant observation noted in *pitx2*^{M6*} adult zebrafish is the formation of ectopic cartilaginous structures appearing to

Table 2. Summary of select downregulated genes

Gene symbol	Human ortholog	Full Name	Human disease, Inheritance Mode, OMIM no., other relevant phenotypes	Ocular tissue enrichment in BioGPS mouse[a]
col1a1a	*COL1A1*	collagen, Type I, alpha 1a	Caffey disease, AD, 114000; EDS, classic and type VIIA, AD, 130000 and 130060; OI, Types I–IV, fAD, 166200, 166210, 259420, and 166220; glaucoma (49–52)	**Eyecup; iris, ciliary bodies, cornea**
col1a2	*COL1A2*	collagen, Type I, alpha 2	EDS, cardiac valvular form, AR, 225320; EDS, type VIIB, AD, 130060; OI, Types II–IV, AD, 166210, 259420, and 166220;	**Eyecup;** ciliary bodies
col5a2b	*COL5A2*	collagen, Type V, alpha 2b	EDS, classic type, AD, 130000	**Eyecup**; **iris**; ciliary bodies, cornea
col5a3b	*COL5A3*	collagen, Type V, alpha 3b	Partial deletions of *COL5A3* and *OLFM2* identified in a patient with bilateral microphthalmia, sclerocornea, and ptosis, small teeth, bifid uvula, hearing and other defects (46)	Not enriched
tert	*TERT*	telomerase reverse transcriptase	Dyskeratosis congenita, AD/AR, 613989; Leukemia, acute myeloid, AD, 601626; Melanoma, cutaneous malignant, 9, 615134; Pulmonary fibrosis and/or bone marrow failure, 1, AD, 614742	Ciliary bodies, lens
wnt3	*WNT3*	wingless-type MMTV integration site family, member 3	Tetra-amelia syndrome, AR, 273395	Not enriched
wnt4a	*WNT4*	wingless-type MMTV integration site family, member 4a	SERKAL syndrome, AR, 611812; Mullerian aplasia and hyperandrogenism, AD, 158330	**Cornea;** ciliary bodies, eyecup, lens
wnt6b	*WNT6*	wingless-type MMTV integration site family, member 6b	None	Iris
wnt7aa	*WNT7A*	wingless-type MMTV integration site family, member 7aa	Fuhrmann syndrome, AR, 228930; Ulna and fibula, absence of, with severe limb deficiency, AR, 276820; loss of WNT7A induces limbal stem cells into skin-like epithelium (76)	**Lens**; **cornea;** retinal pigment epithelium
wnt9b	*WNT9B*	wingless-type MMTV integration site family, member 9b	None	Not enriched
wnt10a	*WNT10A*	wingless-type MMTV integration site family, member 10a	Odontoonychodermal dysplasia, AR, 257980; Schopf-Schulz-Passarge syndrome, AR, 224750; Tooth agenesis, selective, 4, AD/AR, 150400; decrease in central corneal thickness in humans (77)	**Iris, cornea;** ciliary bodes, eyecup

[a]Ocular structures showing an enrichment of at least 3× over median expression level for at least one probe set are indicated; tissues showing 10× enrichment are highlighted in **bold,** and those with 30× enrichment are **underlined** as well (BioGPS.org).

arise from the limbus and extend into the presumptive cornea. It could be hypothesized that *pitx2* within the ocular mesenchyme serves not only to maintain corneal identity but also to counteract aberrant cartilage formation, so that when depleted, the mesenchyme and surrounding cells shift their fate to skin and cartilage. An alternative hypothesis is that presumptive iris stroma or corneal endothelial cells are failing to properly differentiate but instead either become and/or maintain a multipotent state followed by inappropriate differentiation into melanocytes, cartilage, and skin at later stages (63).

A final notable feature of *pitx2*^{M64*} animals is a reduced or absent posterior vitreous chamber that, together with the lack of anterior chamber, leads to an overall more compressed appearance to the eye. In mammals, the vitreous body is an extracellular matrix reservoir of basal membrane proteins derived from the ciliary body and lens (64,65). The vitreous body of zebrafish should be developed by 1 mpf and is delineated from the anterior chamber by the formation of lens zonules (32). Though it has not been studied in zebrafish, the failure of proper ciliary zone differentiation in *pitx2*^{M64*} mutants may account for the absence/reduction of the vitreous body due to the lack of secreted vitreous components. The most commonly noted posterior defect in ARS patients is glaucomatous cupping of the optic nerve head, which is believed to develop in response to the increased IOP. However, a literature search identified several reports that presented additional posterior segment anomalies in ARS. A 'primary vitreous condensation' was noted in four individuals with ARS and a 'predicted to be pathogenic' variant in *PRDM5* (66). For *PITX2*-positive ARS, a few reports indicated the presence of Persistent Hyperplastic Primary Vitreous (PHPV) and retinal detachment associated with proliferative vitreoretinopathy (67,68). PHPV is a congenital disorder characterized by a failure of the early embryonic vasculature of the eye to regress during development, causing a white vascularized tissue to remain behind the lens and leading to retinal detachment in many cases (69). Additional studies are needed to better understand the possible role of PITX2/pitx2 in the vitreous/posterior segment and its significance for glaucoma development.

In humans, ARS is caused by *PITX2* haplo-insufficiency, while heterozygous *pitx2*^{M64*} fish appear to be grossly normal.

These distinctions may be attributed to differences in *PITX2*/*pitx2* dosage requirements between species. Homozygous mutations in human *PITX2* have not been reported but are likely to result in more severe ocular malformations, possibly resembling the spectrum observed in *pitx2*^{M64*} homozygous animals. There is evidence to suggest that some *PITX2*-positive cases affected with a more severe phenotype may have a greater disruption of PITX2 function. For example, a more severe phenotype was identified in a patient with a dominant-negative mutation in *PITX2* (70). In addition, patients carrying mutations in both *PITX2* and *FOXC1*, shown to result in a cumulative effect with greater loss of function, displayed severe ASD with corneal opacification, peripheral corneal vascularization, and PHPV ultimately resulting in bilateral retinal detachment (71). Histological analysis of the affected cornea showed corneal epithelium focal thickening and basal vacuolation, stromal vascularization, stromal collagen fiber separation due to accumulation of mucopolysaccharide-like ground substance, and partially or fully absent Bowman's layer, Descemet's membrane, and endothelium (71). It is also interesting to note that, even though the visible abnormal phenotypes in zebrafish are present starting at embryonic stage 3-dpf, the features become more severe as animals age. Although ARS in human patients is often diagnosed at birth (with features like, iris hypoplasia/iris processes being notable at that point), some attributes (like increased IOP and glaucoma) are known to develop with age. It is possible that phenotypic progression in humans involves additional ocular features that have not yet been recognized due to the lack of longitudinal studies.

Transcriptome analyses to identify ocular factors that are dependent on normal *pitx2* expression during early eye development revealed numerous transcripts, with several selected genes of WNT and collagen families verified by quantitative PCR. As discussed earlier, the link between the Wnt pathway and Pitx2 has been previously identified. Not only has the Wnt/Disheveled/β-catenin pathway been shown to both directly induce *Pitx2* expression and stabilize *Pitx2* mRNA in a cell-type-specific manner, but Pitx2 has also been demonstrated to regulate Wnt pathway ligands, receptors, and antagonists (21,72–74). PITX2 was found to interact with the promoters of five WNT ligands and induce expression of four of the ligands leading to activation of the β-catenin-dependent canonical Wnt pathway and enhanced cell proliferation in cancer cell lines (74). A zebrafish ortholog of one of the induced ligands, *WNT6*, was also identified by our microarray; moreover, *WNT6* was also previously detected as a FOXC1 target in two independent assays (75) and thus may represent a common downstream target of two ARS factors. Also among the human orthologs of our microarray targets, WNT7A has been shown to induce limbal stem cells into skin-like epithelium when depleted (76), and an exonic variant in WNT10A has been implicated in decreasing central corneal thickness and doubling the risk of keratoconus in humans (77). While PITX2 was shown to exhibit a positive feedback control loop with WNT ligands, its overexpression was demonstrated to reduce the expression of several Frizzled receptors and lipoprotein receptor-related protein (LRP) co-receptors, thus suggesting that it also supplies negative feedback control to the pathway (74). Such negative regulation is consistent with the observation of the activation by Pitx2 of certain Wnt antagonists like *Dkk2* (21). Further testing will be needed to verify if Pitx2 is a direct regulator of the identified Wnt ligands and antagonists or if the observed down-regulation of both in *pitx2* mutants is a compensatory mechanism in which one class is directly targeted and the other fluctuates in response.

Another group of targets with significant down-regulation in *pitx2* mutant eyes were transcripts encoding for collagens I and V. Collagen I is the primary component of the orthogonally arranged, stratified fibril layers that make up the vertebrate corneal stroma, and collagen V is a key support molecule for collagen I fibril formation (43,78). Mutations in collagens have been identified as causative of Ehlers-Danlos syndromes (EDS), a genetically heterogeneous group of connective tissue disorders (47,79). In particular: mutations in *COL1A1* (rare) and *COL5A2* (major) are associated with classic EDS [MIM 130000] (79); mutations in *COL1A1* and *COL1A2* are associated with EDS, arthrochalasia type [MIM 130060] (79–81); and *COL1A2* mutations are also associated with EDS cardiac valvular type [MIM 225320]. EDS exhibits several features that overlap findings present in ARS patients, including (but not limited to): microcornea; glaucoma; cornea plana; small, irregularly placed teeth; umbilical and inguinal hernias; mitral valve prolapse; and hyperextensibility (47,82). Mutations in *COL1A1* have been associated with various glaucoma phenotypes, including both primary open angle and infantile-onset/primary congenital; the majority of patients with these phenotypes also presented with osteogenesis imperfecta (OI), a group of inherited disorders characterized primarily by fragile bones and secondarily with mitral valve prolapse, blue sclerae, thin corneas, optic atrophy, vitreous hyperplasia and corneal opacities, among other features (49–51). Interestingly, one case of OI with features of both EDS and ARS has been attributed to a frameshift c.3313delA mutation in *COL1A1* (52), further linking these two phenotypes. Finally, a partial deletion involving another collagen gene, *COL5A3*, and *OLFM2* was recently identified in a patient with bilateral microphthalmia, sclerocornea, ptosis, small teeth, bifid uvula and hearing defects (46). Our work suggests that PITX2/pitx2 may regulate expression of genes encoding collagens I and V. With this, early deficiency in expression of corneal collagens is likely to contribute to the abnormal phenotypes associated with *PITX2*/*pitx2* disruption. Further work will determine whether the down-regulation of collagen transcripts is a result of direct involvement of pitx2 in regulation of their expression or a secondary effect.

Overall, the developed *pitx2*^{M64*} zebrafish line recapitulates the characteristic phenotypes of *PITX2*-mediated ARS. In addition to this, the possible role of *PITX2* in corneal dermoid phenotypes is further supported by the presented zebrafish data. The initial molecular assessment of *pitx2*-deficient ocular tissues at early stages of development, prior to structural defects, identified significant changes in the expression of multiple Wnt and collagen genes, some of which have been previously associated with overlapping ocular and craniofacial phenotypes. The developed model will be useful in examining the mechanisms of a wide range of ocular phenotypes associated with *PITX2* deficiency and identifying potential therapeutic targets.

Materials and Methods

Human screening

This human study was approved by the Institutional Review Board of Children's Hospital of Wisconsin with written informed consent obtained for every subject including consent for photo publication. The diagnosis of ARS was based on clinical evaluation by referring physicians. In general, at least one family member needed to have characteristic ocular findings (posterior embryotoxon, iris processes, iris hypoplasia, pupillary anomalies) with two or more of the typical non-ocular features

(dental, umbilical and/or craniofacial) of ARS. Sequencing of *PITX2* and *FOXC1* was undertaken as previously described in (3). Identified variants were assessed for pathogenicity using the ACMG/AMP guidelines for the interpretation of sequence variants (40). Causative variants were confirmed in the proband through independent Sanger sequencing reactions, and family members were tested for co-segregation when available. Analysis of the predicted effect of missense mutations was undertaken through 5 prediction algorithms—SIFT, PolyPhen2, MutationTaster, MutationAssessor and FATHMM—accessed through the Variant Effect Predictor (http://www.ensembl.org/Tools/VEP). Analysis of variant frequencies in the general population was performed using the gnomAD Browser (genome Aggregation Database; http://gnomad.broadinstitute.org). Mutations were submitted to the LOVD 3.0 shared installation PITX2 database (https://databases.lovd.nl/shared/genes/PITX2).

Development of mutant pitx2 lines via TALEN-mediated genome editing

Zebrafish generation, maintenance and staging were performed as previously described in (37). Embryos were raised with or without 1-phenyl 2-thiourea. TALENs were produced per the protocol of Sanjana *et al.* (83). Briefly, TALENs were designed to target the homeodomain-encoding exon of the *pitx2* gene that is shared by both zebrafish isoforms *pitx2a* (exon 3) and *pitx2c* (exon 2) (left TALEN—5'-TTTCAGAGGAATCGCTATC-3' and right TALEN—5'-AGGAGATCGCCGTTTGGAC-3'). Disruptions in this region were predicted to impact the SalI restriction site (GTCGAC) found between the TALENs. TALEN mRNA was injected into 1–4 cell stage wildtype zebrafish embryos to generate mosaic founders, which when bred generated F1 heterozygous *pitx2* mutant embryos that went on to produce F2 homozygous embryos used for further study. The genomic fragment surrounding the homeobox was PCR-amplified using primers *s*-5'-CCCTCACGCACACTTCTCTA-3' and *a*-5'-GCATTAAGCTGATAGGCTATCTTG-3'. Digestion by SalI-HF (New England Biolabs, Ipswich, MA) established TALEN cutting efficiency and detected four generated mutant lines [c.190_197delATGTCGAC, p.(Met64*); c.193_195delTCG, p.(Ser65del); c.191_196delTGTCGA, p.(Met64_Ser65del); c.191_199delTGTCGACTA, p.(Met64_Thr66del)]. Sanger sequencing confirmed the four potential mutations as well as identified one additional line [c.193_195dupTCG, p.(Ser65dup)].

Characterization of embryonic and adult phenotypes in pitx2 mutants

Alcian Blue cartilage staining was performed as per Barrallo-Gimeno *et al.* (84). Briefly, embryos were collected at 5-dpf and fixed overnight in 4% paraformaldehyde in 1× diethyl pyrocarbonate (DEPC)-phosphate-buffered saline (PBS) at 4°C. Following two PBS washes, embryos were bleached in 1 ml 10% hydrogen peroxide (H_2O_2) supplemented with 50 µl of 2M KOH for 1 h on a rotating platform. Embryos were stained overnight in 0.1% Alcian Blue solution comprised of Alcian Blue 8GX (Sigma-Aldrich, St Louis, MO) dissolved in acidic ethanol. Stained embryos were washed thoroughly with acidic ethanol, digested in proteinase K for 1 h, re-fixed in 4% paraformaldehyde, progressively dehydrated with ethanol, and stored in 80% glycerol at 4°C. Craniofacial structures were identified as presented by Piotrowski *et al.* (85). Whole mount images were obtained on a Nikon SMZ1500 dissection microscope (Nikon Instruments Inc., Melville, NY).

Electron microscopy was performed as described by Soules and Link (32). Briefly, 3- and 14-dpf embryos were collected and fixed in primary fixative [2% paraformaldehyde, 2.5% glutaraldehyde, 3% sucrose, 0.06% phosphate buffer (pH 7.4)] at 4°C. Specimens were submitted to the Electron Microscopy Facility at the Medical College of Wisconsin for embedding, which included 1-h post-fixation in 1% osmium tetroxide on ice for membrane preservation, dehydration through a series of methanol and acetonitrile washes, and infiltration with EMbed 812 resin (14120; Electron Microscopy Sciences, Hatfield, PA). Transverse, semi-thin (500 nm) sections were cut with a DiATOME Histo diamond knife (HI10213; DiATOME, Hatfield, PA) on a PowerTome XL microtome (Boeckeler Instruments, Tucson, AZ) and collected throughout the central anterior chamber as defined by maximum lens diameter. Sections were heat-fixed to glass slides, stained with 1% Toluidine Blue in 1% Borax buffer, and imaged on an AxioImager.Z1 microscope with an AxioCam MRc5 camera and ZEN pro software (Zeiss, Thornwood, NY). Ultrathin sections (70–80 nm) were subsequently taken at ∼ 3–5 µm intervals through the central anterior chamber with a DiATOME Ultra 45° diamond knife (MT7376; DiATOME), collected on copper hexagonal mesh coated grids (G200H-Cu; Electron Microscopy Sciences) and stained with uranyl acetate and lead citrate for contrast. Images were captured using a Hitachi H600 TEM microscope (Hitachi, Tokyo, Japan).

Inclusion body count and area measurements were performed with ImageJ software (https://imagej.nih.gov/ij/). Electron microscopy images of 3-dpf dorsal, central and ventral cornea for a wild-type and mutant embryo at the same magnification were used. Inclusion bodies were designated as electron-dense structures in the corneal surface epithelial and subepithelial layers that did not appear to be membrane-bound or within a membrane-bound organelle. All inclusion bodies identified in wild-type or mutant images in either surface or subepithelial layers were measured; the data from three images were pooled together and displayed as a box and whisker plot for each condition (wild-type versus mutant) for each epithelial layer. The statistical significance of average inclusion body area per layer between wild-type and mutant images was determined using the Student's t-test.

For histology, 1-mpf and 1- to 2-year-old adult fish tissues were preserved in 10% formalin and submitted to the Children's Research Institute Histology Core at the Medical College of Wisconsin for paraffin sectioning and H&E staining per standard protocols. Slides were imaged on a NanoZoomer digital slide scanner, and images were viewed with NDP.view2 viewing software (Hamamatsu, Hamamatsu City, Japan).

PAS staining was performed per standard protocols. 1-mpf and adult paraffin sections were immersed in 1% acid alcohol [hydrochloric acid and 70% alcohol] for 5 min to de-colorize following H&E staining. Slides were oxidized in 0.5% periodic acid for 5 min, rinsed in distilled water, and stained with Schiff's reagent (Newcomer Supply, Middleton, WI) for 15 min. Sections were rinsed in warm tap water for 7 min then in distilled water before being counterstained with hematoxylin for 1 min and rinsed again. Slides were placed in clarifier for 30 s then rinsed 1 min each in distilled water, 0.1% ammonia water, and distilled water; they were quickly dehydrated through two changes of 95% alcohol, three of 100% alcohol and three of xylene before cover-slipping and imaging as described earlier.

For immunohistochemistry, 1-mpf and 1- to 2-year-old adult paraffin sections on cover-slipped slides were soaked in xylene for 2–3 days to remove the coverslip. Paraffin sections

were exposed to antigen retrieval for 10–20 min at 100°C then kept at room temperature for 20-min followed by two 5-min water rinses and one 10-min PBS plus 0.1% Tween-20 (PBT) wash. Slides were blocked in 10% donkey serum for 2 h and incubated in primary antibody overnight at 4°C. Slides underwent two 10-min PBT washes followed by a 2-h incubation in secondary antibody and imaging as previously described. Primary antibodies utilized were collagen 1a1a (col1a1a; 1:100; GTX124368; GeneTex, Inc., Irvine, CA), CKS proteoglycan (1:200; MAB2022; EMD Millipore, Billerica, MA), N-cadherin (cdh2; 1: 50, GTX125962; GeneTex) and DAPI (1:1000; 62247; Thermo Fisher Scientific, Waltham, MA). Secondary antibodies used were donkey anti-rabbit Alexa Fluor 488 IgG (1:100; A-21206; Thermo Fisher) and donkey anti-mouse Alexa Fluor 568 IgG (1:100; A-10037; Thermo Fisher).

For ISH and TUNEL staining, embryos underwent standard fixation protocols. Embryos were collected at the desired stage, washed twice with 1× DEPC-PBS and fixed overnight in 4% paraformaldehyde in DEPC-PBS at 4°C. Embryos underwent two 5-min ice cold PBS washes and four 5-min ice cold 100% methanol washes then were stored at −20°C.

ISH was performed as previously described in (37). A *foxc1a* plasmid was ordered from Open Biosystems (8001422; GE Dharmacon, Lafayette, CO) and linearized with EcoRI (New England Biolabs). An 843-bp *foxc1a* digoxigenin-labeled antisense RNA probe was generated using the DIG RNA labeling mix from Roche Diagnostics and T7 RNA polymerase (Roche Diagnostics Corporation, Indianapolis, IN). Whole mount embryos were imaged as described above.

RNAscope probe Dr-Pitx2 (467531-C1; Advanced Cell Diagnostics, Newark, CA) was obtained and used as described by Gross-Thebing *et al.* (86). For cryosectioning, stained embryos were prepared by undergoing: two PBS washes; two overnight infiltrations at 4°C, first with 30% sucrose/PBS then with Tissue-Tek O.C.T. Compound (Sakura Finetek USA, Inc., Torrance, CA); embedding in cryomolds; and freezing. 10-micron sections were obtained using a Microm HM550 cryostat (Thermo Fisher), melted onto charged glass slides, mounted with ProLong Gold antifade reagent (Invitrogen Corporation, Carlsbad, CA), and imaged as previously described.

TUNEL staining was performed as described by Eimon (87) utilizing the In-Situ Apoptosis Detection Kit from Millipore (Merck KGaA, Darmstadt, Germany). Fixed embryos were gradually rehydrated into PBT, digested in 10 μg proteinase K/ml in PBT for 15–45 min (depending on the developmental stage), washed twice in PBT, and fixed in precooled (2:1) ethanol: acetic acid for 10 min at −20°C. Embryos were drained, washed twice in PBT, incubated in ApopTag Equilibration Buffer for 1 h, and incubated with a 70% ApopTag Reaction Buffer + 30% ApopTag TDT Enzyme solution overnight at 37°C. Embryos were washed once in ApopTag stop/wash Buffer [1 ml Stop/Wash Buffer + 34 ml H_2O] for 10 min, blocked in blocking solution [1× PBT, 2% (v/v) sheep serum, 2 mg/ml BSA] for 3–4 h, and incubated overnight in 1:5000 anti-digoxigenin-alkaline phosphatase (AP) Fab antibody (11093274910; Roche) in blocking solution at 4°C with gentle agitation. Embryos underwent eight 15-min PBT washes, three 5-min fresh NTMT (AP) buffer washes [0.1 M Tris-HCL pH 9.5, 50 mM $MgCl_2$, 100 mM NaCl, 0.1% Tween-20], and staining in fresh substrate solution [1.0 ml AP Buffer + 2.25 μl 4-Nitro blue tetrazolium chloride (100 mg/ml; Roche) + 3.5 μl 5-Bromo-4-chloro-3-indolyl-phosphate (50 mg/ml; Roche)] for 10 min to 1 h in the dark. To stop staining, embryos were washed twice with PBT and fixed in 4% paraformaldehyde overnight at 4°C. Embryos underwent two 5-min cold PBT washes and progressive 5-min methanol washes for dehydration and storage (25, 50 and 75% methanol in PBT, 100% methanol twice). For whole mount photography, embryos were exchanged into PBT two times for 15 min then into 80% glycerol and imaged as described above. For post-stain sectioning, embryos underwent cryosectioning and imaging as previously described.

Transcriptome analysis in pitx2^{M64*} embryos

To collect embryonic ocular tissues from mutant and wild-type embryos, whole eyes of 23-hpf embryos were dissected while the remaining tissue was utilized for genotyping. Wild-type and *pitx2*^{M64*} homozygous mutant whole eyes were then pooled together for RNA extractions (final samples contained 56, 58 and 50 eyes for homozygous mutants and 88, 109 and 112 for wild-type tissues). RNA was extracted from the collected eyes using TRIzol and the Direct-zol RNA MiniPrep Kit (Zymo Research, Irvine, CA). RNA quality was assessed on both a NanoDrop 2000 UV-Vis Spectrophotometer (Thermo Fisher) and an Agilent 2100 Bioanalyzer utilizing the Agilent RNA 6000 Pico Kit (Agilent Technologies, Santa Clara, CA). RNA from three independent *pitx2*^{M64*} homozygous eye collections with RNA Integrity Numbers (RINs) of 8.9, 8.6 and 9.0 and three independent wild-type collections with RINs 8.7, 8.9, and 8.7 was submitted to OakLabs (Hennigsdorf, Germany) for transcriptome analysis using an ArrayXS Zebrafish v1 microarray containing 60 023 target IDs. Statistical analysis of the microarray data was performed by Oaklabs and consisted of quantile normalization using ranked median quantiles, conversion to log2 values for calculation of control versus mutant means and standard deviations per target, and Welch's t-test (or unequal variances t-test) that was used to test the hypothesis that the signals of the gene in the two biological groups of samples (e.g. mutant and wild-type) have equal means. Differentially expressed targets were defined as having a change in mean log2 >1 between mutant and wild-type values, correlating to a 2-fold change in expression, and a P-value < 0.05. For pathway analysis, zebrafish-specific transcripts were annotated with human orthologs using Ensembl Biomart (http://useast.ensembl.org/biomart). Remaining transcripts with no identified orthologs were manually annotated by using the provided Ensembl transcript id to search for orthologs or paralogs within Ensembl [http://grch37.ensembl.org/Danio_rerio (Zebrafish Zv9); http://useast.ensembl.org/Danio_rerio (Zebrafish GRCz10)] or to perform a protein BLAST (https://blast.ncbi.nlm.nih.gov). The list of human orthologs was analyzed for pathway enrichment by Ingenuity Pathway Analysis software (Qiagen, Hilden, Germany). Microarray data were submitted to the ArrayExpress database at EMBL-EBI under Accession Number E-MTAB-6463 (www.ebi.ac.uk/arrayexpress).

Select identified targets were verified by real-time quantitative PCR using transcript-specific primers (Supplementary Material, Table S1), SYBR Green PCR Master Mix (Applied Biosystems, Waltham, MA) and CFX Connect and CFX96 Touch Real-Time PCR Detection Systems (Bio Rad, Hercules, CA). 24-, 48- and 72-hpf wild-type and *pitx2*^{M64*} homozygous eye cDNA was generated from equal concentrations of wild-type and *pitx2*^{M64*} homozygous eye RNA utilizing SuperScript III reverse transcriptase (Thermo Fisher). Each experiment included the following conditions at 200 pg cDNA per technical replicate: 24-, 48- or 72-hpf wild-type eye cDNA; 24-, 48- or 72-hpf *pitx2*^{M64*} homozygous eye cDNA; no reverse transcriptase control; and no template control which excluded primers. All samples were

normalized to β-actin and run in triplicate to obtain average Cq values. Total fold changes and standard deviations were calculated as the average of three independent biological repeats via the efficiency-corrected ΔCq model, which accounts for differing primer efficiencies. Statistical significance was determined using the Student's t-test.

For heatmap generation, the collective average and standard deviation of the normalized three wild-type and three *pitx2*^{M64*} replicates for each target of interest were calculated, and the Z-score for each replicate was derived by dividing the difference between the replicate and the mean by the standard deviation. Z-scores were imported into the SNP and Variation Suite software (Golden Helix, Inc., Bozeman, MT) for heatmap synthesis.

Supplementary Material

Supplementary Material is available at *HMG* online.

Acknowledgements

The authors gratefully acknowledge the patients and their families for their participation in research studies. We would also like to thank the Department of Cell Biology, Neurobiology and Anatomy for use of shared equipment, as well as Christine Duris and the Children's Research Institute Histology Core and Clive Wells and Robert Goodwin from the Medical College of Wisconsin Electron Microscopy Core Facility for technical assistance.

Conflict of Interest statement. None declared.

Funding

This work was supported by awards from the National Institutes of Health (EY015518) as well as funds provided by the Children's Research Institute Foundation at Children's Hospital of Wisconsin (E.V.S.), NEI Training Grant (5T32EY014537–13 and -14), and NIH Core Grant (P30EY001931). Funding to pay the Open Access publication charges for this article was provided by the Department of Pediatrics at the Medical College of Wisconsin.

References

1. Semina, E.V., Reiter, R., Leysens, N.J., Alward, W.L., Small, K.W., Datson, N.A., Siegel-Bartelt, J., Bierke-Nelson, D., Bitoun, P., Zabel, B.U. *et al.* (1996) Cloning and characterization of a novel bicoid-related homeobox transcription factor gene, RIEG, involved in Rieger syndrome. *Nat. Genet.*, **14**, 392–399.
2. Reis, L.M. and Semina, E.V. (2011) Genetics of anterior segment dysgenesis disorders. *Curr. Opin. Ophthalmol.*, **22**, 314–324.
3. Reis, L.M., Tyler, R.C., Volkmann Kloss, B.A., Schilter, K.F., Levin, A.V., Lowry, R.B., Zwijnenburg, P.J., Stroh, E., Broeckel, U., Murray, J.C. *et al.* (2012) PITX2 and FOXC1 spectrum of mutations in ocular syndromes. *Eur. J. Hum. Genet.*, **20**, 1224–1233.
4. Alward, W.L. (2000) Axenfeld-Rieger syndrome in the age of molecular genetics. *Am. J. Ophthalmol.*, **130**, 107–115.
5. Strungaru, M.H., Dinu, I. and Walter, M.A. (2007) Genotype-phenotype correlations in Axenfeld-Rieger malformation and glaucoma patients with FOXC1 and PITX2 mutations. *Invest. Ophthalmol. Vis. Sci.*, **48**, 228–237.
6. Tümer, Z. and Bach-Holm, D. (2009) Axenfeld-Rieger syndrome and spectrum of PITX2 and FOXC1 mutations. *Eur. J. Hum. Genet.*, **17**, 1527–1539.
7. Gudbjartsson, D.F., Arnar, D.O., Helgadottir, A., Gretarsdottir, S., Holm, H., Sigurdsson, A., Jonasdottir, A., Baker, A., Thorleifsson, G., Kristjansson, K. *et al.* (2007) Variants conferring risk of atrial fibrillation on chromosome 4q25. *Nature*, **448**, 353–357.
8. Lubitz, S.A., Lunetta, K.L., Lin, H., Arking, D.E., Trompet, S., Li, G., Krijthe, B.P., Chasman, D.I., Barnard, J., Kleber, M.E. *et al.* (2014) Novel genetic markers associate with atrial fibrillation risk in Europeans and Japanese. *J. Am. Coll. Cardiol.*, **63**, 1200–1210.
9. Sun, Y.M., Wang, J., Qiu, X.B., Yuan, F., Xu, Y.J., Li, R.G., Qu, X.K., Huang, R.T., Xue, S. and Yang, Y.Q. (2016) PITX2 loss-of-function mutation contributes to tetralogy of Fallot. *Gene*, **577**, 258–264.
10. Lee, J.Y., Kim, T.H., Yang, P.S., Lim, H.E., Choi, E.K., Shim, J., Shin, E., Uhm, J.S., Kim, J.S., Joung, B. *et al.* (2017) Korean atrial fibrillation network genome-wide association study for early-onset atrial fibrillation identifies novel susceptibility loci. *Eur. Heart J*, **38**, 2586–2594.
11. Liu, L., Ebana, Y., Nitta, J.I., Takahashi, Y., Miyazaki, S., Tanaka, T., Komura, M., Isobe, M. and Furukawa, T. (2017) Genetic variants associated with susceptibility to atrial fibrillation in a Japanese population. *Can. J. Cardiol.*, **33**, 443–449.
12. Xia, K., Wu, L., Liu, X., Xi, X., Liang, D., Zheng, D., Cai, F., Pan, Q., Long, Z., Dai, H. *et al.* (2004) Mutation in PITX2 is associated with ring dermoid of the cornea. *J. Med. Genet.*, **41**, e129.
13. Cox, C.J., Espinoza, H.M., McWilliams, B., Chappell, K., Morton, L., Hjalt, T.A., Semina, E.V. and Amendt, B.A. (2002) Differential regulation of gene expression by PITX2 isoforms. *J. Biol. Chem.*, **277**, 25001–25010.
14. Volkmann, B.A., Zinkevich, N.S., Mustonen, A., Schilter, K.F., Bosenko, D.V., Reis, L.M., Broeckel, U., Link, B.A. and Semina, E.V. (2011) Potential novel mechanism for Axenfeld-Rieger syndrome: deletion of a distant region containing regulatory elements of PITX2. *Invest. Ophthalmol. Vis. Sci.*, **52**, 1450–1459.
15. Flomen, R.H., Vatcheva, R., Gorman, P.A., Baptista, P.R., Groet, J., Barisic, I., Ligutic, I. and Nizetic, D. (1998) Construction and analysis of a sequence-ready map in 4q25: rieger syndrome can be caused by haploinsufficiency of RIEG, but also by chromosome breaks approximately 90 kb upstream of this gene. *Genomics*, **47**, 409–413.
16. Kozlowski, K. and Walter, M.A. (2000) Variation in residual PITX2 activity underlies the phenotypic spectrum of anterior segment developmental disorders. *Hum. Mol. Genet.* **9**, 2131–2139.
17. Espinoza, H.M., Cox, C.J., Semina, E.V. and Amendt, B.A. (2002) A molecular basis for differential developmental anomalies in Axenfeld-Rieger syndrome. *Hum. Mol. Genet.*, **11**, 743–753.
18. Maciolek, N.L., Alward, W.L., Murray, J.C., Semina, E.V. and McNally, M.T. (2006) Analysis of RNA splicing defects in PITX2 mutants supports a gene dosage model of Axenfeld-Rieger syndrome. *BMC Med. Genet.*, **7**, 59.
19. Priston, M., Kozlowski, K., Gill, D., Letwin, K., Buys, Y., Levin, A.V., Walter, M.A. and Heon, E. (2001) Functional analyses of two newly identified PITX2 mutants reveal a novel molecular mechanism for Axenfeld-Rieger syndrome. *Hum. Mol. Genet.*, **10**, 1631–1638.
20. Saadi, I., Toro, R., Kuburas, A., Semina, E., Murray, J.C. and Russo, A.F. (2006) An unusual class of PITX2 mutations in

Axenfeld-Rieger syndrome. *Birth Defects Res. A. Clin. Mol. Teratol.*, **76**, 175–181.
21. Gage, P.J., Qian, M., Wu, D. and Rosenberg, K.I. (2008) The canonical wnt signaling antagonist DKK2 is an essential effector of PITX2 function during normal eye development. *Dev. Biol.*, **317**, 310–324.
22. Chen, L., Martino, V., Dombkowski, A., Williams, T., West-Mays, J. and Gage, P.J. (2016) AP-2beta is a downstream effector of PITX2 required to specify endothelium and establish angiogenic privilege during corneal development. *Invest. Ophthalmol. Vis. Sci.*, **57**, 1072–1081.
23. Green, P.D., Hjalt, T.A., Kirk, D.E., Sutherland, L.B., Thomas, B.L., Sharpe, P.T., Snead, M.L., Murray, J.C., Russo, A.F. and Amendt, B.A. (2001) Antagonistic regulation of Dlx2 expression by PITX2 and Msx2: implications for tooth development. *Gene Expr.*, **9**, 265–281.
24. Mears, A.J., Jordan, T., Mirzayans, F., Dubois, S., Kume, T., Parlee, M., Ritch, R., Koop, B., Kuo, W.L., Collins, C. *et al.* (1998) Mutations of the forkhead/winged-helix gene, FKHL7, in patients with Axenfeld-Rieger anomaly. *Am. J. Hum. Genet.*, **63**, 1316–1328.
25. Nishimura, D.Y., Swiderski, R.E., Alward, W.L., Searby, C.C., Patil, S.R., Bennet, S.R., Kanis, A.B., Gastier, J.M., Stone, E.M. and Sheffield, V.C. (1998) The forkhead transcription factor gene FKHL7 is responsible for glaucoma phenotypes which map to 6p25. *Nat. Genet.*, **19**, 140–147.
26. Berry, F.B., Lines, M.A., Oas, J.M., Footz, T., Underhill, D.A., Gage, P.J. and Walter, M.A. (2006) Functional interactions between FOXC1 and PITX2 underlie the sensitivity to FOXC1 gene dose in Axenfeld-Rieger syndrome and anterior segment dysgenesis. *Hum. Mol. Genet.*, **15**, 905–919.
27. Gage, P.J., Suh, H. and Camper, S.A. (1999) Dosage requirement of Pitx2 for development of multiple organs. *Development*, **126**, 4643–4651.
28. Kitamura, K., Miura, H., Miyagawa-Tomita, S., Yanazawa, M., Katoh-Fukui, Y., Suzuki, R., Ohuchi, H., Suehiro, A., Motegi, Y., Nakahara, Y. *et al.* (1999) Mouse Pitx2 deficiency leads to anomalies of the ventral body wall, heart, extra- and perioocular mesoderm and right pulmonary isomerism. *Development*, **126**, 5749–5758.
29. Lu, M.F., Pressman, C., Dyer, R., Johnson, R.L. and Martin, J.F. (1999) Function of Rieger syndrome gene in left-right asymmetry and craniofacial development. *Nature*, **401**, 276–278.
30. Lin, C.R., Kioussi, C., O'Connell, S., Briata, P., Szeto, D., Liu, F., Izpisua-Belmonte, J.C. and Rosenfeld, M.G. (1999) Pitx2 regulates lung asymmetry, cardiac positioning and pituitary and tooth morphogenesis. *Nature*, **401**, 279–282.
31. Chen, L. and Gage, P.J. (2016) Heterozygous Pitx2 null mice accurately recapitulate the ocular features of Axenfeld-Rieger syndrome and congenital glaucoma. *Invest. Ophthalmol. Vis. Sci.*, **57**, 5023–5030.
32. Soules, K.A. and Link, B.A. (2005) Morphogenesis of the anterior segment in the zebrafish eye. *BMC Dev. Biol.*, **5**, 12.
33. Zhao, X.C., Yee, R.W., Norcom, E., Burgess, H., Avanesov, A.S., Barrish, J.P. and Malicki, J. (2006) The zebrafish cornea: structure and development. *Invest. Ophthalmol. Vis. Sci.*, **47**, 4341–4348.
34. Link, B.A., Gray, M.P., Smith, R.S. and John, S.W. (2004) Intraocular pressure in zebrafish: comparison of inbred strains and identification of a reduced melanin mutant with raised IOP. *Invest. Ophthalmol. Vis. Sci.*, **45**, 4415–4422.
35. Puzzolo, D., Pisani, A., Malta, C., Santoro, G., Meduri, A., Abbate, F., Montalbano, G., Wylegala, E., Rana, R.A., Bucchieri, F. *et al.* (2018) Structural, ultrastructural, and morphometric study of the zebrafish ocular surface: a model for human corneal diseases?. *Curr. Eye Res.*, **43**, 175–185.
36. Gray, M.P., Smith, R.S., Soules, K.A., John, S.W. and Link, B.A. (2009) The aqueous humor outflow pathway of zebrafish. *Invest. Ophthalmol. Vis. Sci.*, **50**, 1515–1521.
37. Liu, Y. and Semina, E.V. (2012) Pitx2 deficiency results in abnormal ocular and craniofacial development in zebrafish. *PLoS One*, **7**, e30896.
38. Ji, Y., Buel, S.M. and Amack, J.D. (2016) Mutations in zebrafish pitx2 model congenital malformations in Axenfeld-Rieger syndrome but do not disrupt left-right placement of visceral organs. *Dev. Biol.*, **416**, 69–81.
39. Protas, M.E., Weh, E., Footz, T., Kasberger, J., Baraban, S.C., Levin, A.V., Katz, L.J., Ritch, R., Walter, M.A., Semina, E.V. *et al.* (2017) Mutations of conserved non-coding elements of PITX2 in patients with ocular dysgenesis and developmental glaucoma. *Hum. Mol. Genet.*, **26**, 3630–3638.
40. Richards, S., Aziz, N., Bale, S., Bick, D., Das, S., Gastier-Foster, J., Grody, W.W., Hegde, M., Lyon, E., Spector, E. *et al.* (2015) Standards and guidelines for the interpretation of sequence variants: a joint consensus recommendation of the American College of Medical Genetics and Genomics and the Association for Molecular Pathology. *Genet. Med.*, **17**, 405–424.
41. Yin, H.F., Fang, X.Y., Jin, C.F., Yin, J.F., Li, J.Y., Zhao, S.J., Miao, Q. and Song, F.W. (2014) Identification of a novel frameshift mutation in PITX2 gene in a Chinese family with Axenfeld-Rieger syndrome. *J. Zhejiang Univ. Sci. B*, **15**, 43–50.
42. Erdmann, B., Kirsch, F.P., Rathjen, F.G. and More, M.I. (2003) N-cadherin is essential for retinal lamination in the zebrafish. *Dev. Dyn.*, **226**, 570–577.
43. Michelacci, Y.M. (2003) Collagens and proteoglycans of the corneal extracellular matrix. *Braz. J. Med. Biol. Res.*, **36**, 1037–1046.
44. Amendt, B.A., Sutherland, L.B. and Russo, A.F. (1999) Multifunctional role of the Pitx2 homeodomain protein C-terminal tail. *Mol. Cell. Biol.*, **19**, 7001–7010.
45. Park, J.I., Venteicher, A.S., Hong, J.Y., Choi, J., Jun, S., Shkreli, M., Chang, W., Meng, Z., Cheung, P., Ji, H. *et al.* (2009) Telomerase modulates wnt signalling by association with target gene chromatin. *Nature*, **460**, 66–72.
46. Holt, R., Ugur Iseri, S.A., Wyatt, A.W., Bax, D.A., Gold Diaz, D., Santos, C., Broadgate, S., Dunn, R., Bruty, J., Wallis, Y. *et al.* (2017) Identification and functional characterisation of genetic variants in OLFM2 in children with developmental eye disorders. *Hum. Genet.*, **136**, 119–127.
47. Beighton, P., De Paepe, A., Steinmann, B., Tsipouras, P. and Wenstrup, R.J. (1998) Ehlers-Danlos syndromes: revised nosology, Villefranche, 1997. Ehlers-Danlos National Foundation (USA) and Ehlers-Danlos Support Group (UK). *Am. J. Med. Genet.*, **77**, 31–37.
48. Hjalt, T.A. and Semina, E.V. (2005) Current molecular understanding of Axenfeld-Rieger syndrome. *Expert Rev. Mol. Med.*, **7**, 1–17.
49. Wallace, D.J., Chau, F.Y., Santiago-Turla, C., Hauser, M., Challa, P., Lee, P.P., Herndon, L.W. and Allingham, R.R. (2014) Osteogenesis imperfecta and primary open angle glaucoma: genotypic analysis of a new phenotypic association. *Mol. Vis.*, **20**, 1174–1181.
50. Mauri, L., Uebe, S., Sticht, H., Vossmerbaeumer, U., Weisschuh, N., Manfredini, E., Maselli, E., Patrosso, M., Weinreb, R.N., Penco, S. *et al.* (2016) Expanding the clinical spectrum of COL1A1 mutations in different forms of glaucoma. *Orphanet J. Rare Dis.*, **11**, 108–016. 0495-y.

51. Bohnsack, B.L. (2016) Infantile-onset glaucoma and anterior megalophthalmos in osteogenesis imperfecta. *J. Aapos*, **20**, 170–172.
52. Nwosu, B.U., Raygada, M., Tsilou, E.T., Rennert, O.M. and Stratakis, C.A. (2005) Rieger's anomaly and other ocular abnormalities in association with osteogenesis imperfecta and a COL1A1 mutation. *Ophthalmic Genet.*, **26**, 135–138.
53. Amendt, B.A. (2005) *The Molecular Mechanisms of Axenfeld-Rieger Syndrome*. Landes Bioscience/Eurekah.com, Texas.
54. Lines, M.A., Kozlowski, K., Kulak, S.C., Allingham, R.R., Heon, E., Ritch, R., Levin, A.V., Shields, M.B., Damji, K.F., Newlin, A. *et al.* (2004) Characterization and prevalence of PITX2 microdeletions and mutations in Axenfeld-Rieger malformations. *Invest. Ophthalmol. Vis. Sci.*, **45**, 828–833.
55. Kniestedt, C., Taralczak, M., Thiel, M.A., Stuermer, J., Baumer, A. and Gloor, B.P. (2006) A novel PITX2 mutation and a polymorphism in a 5-generation family with Axenfeld-Rieger anomaly and coexisting Fuchs' endothelial dystrophy. *Ophthalmology*, **113**, 1791–1791.e8.
56. Oliveira, M.B., Mitraud, R.S. and Yamane, R. (2008) Axenfeld-Rieger anomaly and corneal endothelial dystrophy: a case series. *Rev. Brasil. Oftalmol.*, **67**, 303–308.
57. Syeda, F., Kirchhof, P. and Fabritz, L. (2017) PITX2-dependent gene regulation in atrial fibrillation and rhythm control. *J. Physiol.*, **595**, 4019–4026.
58. Gage, P.J., Kuang, C. and Zacharias, A.L. (2014) The homeodomain transcription factor PITX2 is required for specifying correct cell fates and establishing angiogenic privilege in the developing cornea. *Dev. Dyn.*, **243**, 1391–1400.
59. Mukhopadhyay, M., Gorivodsky, M., Shtrom, S., Grinberg, A., Niehrs, C., Morasso, M.I. and Westphal, H. (2006) Dkk2 plays an essential role in the corneal fate of the ocular surface epithelium. *Development*, **133**, 2149–2154.
60. Doerdelmann, T., Kojetin, D.J., Baird-Titus, J.M. and Rance, M. (2011) 1H, 13C and 15N chemical shift assignments for the human Pitx2 homeodomain and a R24H homeodomain mutant. *Biomol. NMR Assign.*, **5**, 105–107.
61. Doerdelmann, T., Kojetin, D.J., Baird-Titus, J.M., Solt, L.A., Burris, T.P. and Rance, M. (2012) Structural and biophysical insights into the ligand-free Pitx2 homeodomain and a ring dermoid of the cornea inducing homeodomain mutant. *Biochemistry*, **51**, 665–676.
62. Mattos, J., Contreras, F. and O'Donnell, F.E. Jr (1980) Ring dermoid syndrome. A new syndrome of autosomal dominantly inherited, bilateral, annular limbal dermoids with corneal and conjunctival extension. *Arch. Ophthalmol.*, **98**, 1059–1061.
63. Kikuchi, M., Hayashi, R., Kanakubo, S., Ogasawara, A., Yamato, M., Osumi, N. and Nishida, K. (2011) Neural crest-derived multipotent cells in the adult mouse iris stroma. *Genes Cells*, **16**, 273–281.
64. Bishop, P.N., Takanosu, M., Le Goff, M. and Mayne, R. (2002) The role of the posterior ciliary body in the biosynthesis of vitreous humour. *Eye (Lond)*, **16**, 454–460.
65. Halfter, W., Dong, S., Dong, A., Eller, A.W. and Nischt, R. (2008) Origin and turnover of ECM proteins from the inner limiting membrane and vitreous body. *Eye (Lond)*, **22**, 1207–1213.
66. Micheal, S., Siddiqui, S.N., Zafar, S.N., Venselaar, H., Qamar, R., Khan, M.I. and den Hollander, A.I. (2016) Whole exome sequencing identifies a heterozygous missense variant in the PRDM5 gene in a family with Axenfeld-Rieger syndrome. *Neurogenetics*, **17**, 17.
67. Arikawa, A., Yoshida, S., Yoshikawa, H., Ishikawa, K., Yamaji, Y., Arita, R.I., Ueno, A. and Ishibashi, T. (2010) Case of novel PITX2 gene mutation associated with peters' anomaly and persistent hyperplastic primary vitreous. *Eye (Lond)*, **24**, 391–393.
68. Song, W. and Hu, X. (2017) The rare Axenfeld-Rieger syndrome with systemic anomalies: a case report and brief review of literature. *Medicine (Baltimore)*, **96**, e7791.
69. Shastry, B.S. (2009) Persistent hyperplastic primary vitreous: congenital malformation of the eye. *Clin. Exp. Ophthalmol.*, **37**, 884–890.
70. Saadi, I., Semina, E.V., Amendt, B.A., Harris, D.J., Murphy, K.P., Murray, J.C. and Russo, A.F. (2001) Identification of a dominant negative homeodomain mutation in Rieger syndrome. *J. Biol. Chem.*, **276**, 23034–23041.
71. Kelberman, D., Islam, L., Holder, S.E., Jacques, T.S., Calvas, P., Hennekam, R.C., Nischal, K.K. and Sowden, J.C. (2011) Digenic inheritance of mutations in FOXC1 and PITX2: correlating transcription factor function and Axenfeld-Rieger disease severity. *Hum. Mutat.*, **32**, 1144–1152.
72. Kioussi, C., Briata, P., Baek, S.H., Rose, D.W., Hamblet, N.S., Herman, T., Ohgi, K.A., Lin, C., Gleiberman, A., Wang, J. *et al.* (2002) Identification of a wnt/dvl/beta-catenin –> Pitx2 pathway mediating cell-type-specific proliferation during development. *Cell*, **111**, 673–685.
73. Briata, P., Ilengo, C., Corte, G., Moroni, C., Rosenfeld, M.G., Chen, C.Y. and Gherzi, R. (2003) The wnt/beta -catenin–>Pitx2 pathway controls the turnover of Pitx2 and other unstable mRNAs. *Mol. Cell*, **12**, 1201–1211.
74. Basu, M. and Roy, S.S. (2013) Wnt/beta-catenin pathway is regulated by PITX2 homeodomain protein and thus contributes to the proliferation of human ovarian adenocarcinoma cell, SKOV-3. *J. Biol. Chem.*, **288**, 4355–4367.
75. Tamimi, Y., Lines, M., Coca-Prados, M. and Walter, M.A. (2004) Identification of target genes regulated by FOXC1 using nickel agarose-based chromatin enrichment. *Invest. Ophthalmol. Vis. Sci.*, **45**, 3904–3913.
76. Ouyang, H., Xue, Y., Lin, Y., Zhang, X., Xi, L., Patel, S., Cai, H., Luo, J., Zhang, M., Zhang, M. *et al.* (2014) WNT7A and PAX6 define corneal epithelium homeostasis and pathogenesis. *Nature*, **511**, 358–361.
77. Cuellar-Partida, G., Springelkamp, H., Lucas, S.E., Yazar, S., Hewitt, A.W., Iglesias, A.I., Montgomery, G.W., Martin, N.G., Pennell, C.E., van Leeuwen, E.M. *et al.* (2015) WNT10A exonic variant increases the risk of keratoconus by decreasing corneal thickness. *Hum. Mol. Genet.*, **24**, 5060–5068.
78. Ihanamaki, T., Pelliniemi, L.J. and Vuorio, E. (2004) Collagens and collagen-related matrix components in the human and mouse eye. *Prog. Retin. Eye Res.*, **23**, 403–434.
79. Malfait, F., Francomano, C., Byers, P., Belmont, J., Berglund, B., Black, J., Bloom, L., Bowen, J.M., Brady, A.F., Burrows, N.P. *et al.* (2017) The 2017 international classification of the Ehlers-Danlos syndromes. *Am. J. Med. Genet. C. Semin. Med. Genet.*, **175**, 8–26.
80. Klaassens, M., Reinstein, E., Hilhorst-Hofstee, Y., Schrander, J.J., Malfait, F., Staal, H., ten Have, L.C., Blaauw, J., Roggeveen, H.C., Krakow, D. *et al.* (2012) Ehlers-Danlos arthrochalasia type (VIIA-B)–expanding the phenotype: from prenatal life through adulthood. *Clin. Genet.*, **82**, 121–130.
81. Melis, D., Cappuccio, G., Ginocchio, V.M., Minopoli, G., Valli, M., Corradi, M. and Andria, G. (2012) Cardiac valve disease: an unreported feature in Ehlers Danlos syndrome arthrocalasia type? *Ital. J. Pediatr.*, **38**, 65.

82. Hjalt, T.A., Amendt, B.A. and Murray, J.C. (2001) PITX2 regulates procollagen lysyl hydroxylase (PLOD) gene expression: implications for the pathology of Rieger syndrome. *J. Cell Biol.*, **152**, 545–552.
83. Sanjana, N.E., Cong, L., Zhou, Y., Cunniff, M.M., Feng, G. and Zhang, F. (2012) A transcription activator-like effector toolbox for genome engineering. *Nat. Protoc.*, **7**, 171–192.
84. Barrallo-Gimeno, A., Holzschuh, J., Driever, W. and Knapik, E.W. (2004) Neural crest survival and differentiation in zebrafish depends on mont blanc/tfap2a gene function. *Development*, **131**, 1463–1477.
85. Piotrowski, T., Schilling, T.F., Brand, M., Jiang, Y.J., Heisenberg, C.P., Beuchle, D., Grandel, H., van Eeden, F.J., Furutani-Seiki, M., Granato, M. *et al.* (1996) Jaw and branchial arch mutants in zebrafish II: anterior arches and cartilage differentiation. *Development*, **123**, 345–356.
86. Gross-Thebing, T., Paksa, A. and Raz, E. (2014) Simultaneous high-resolution detection of multiple transcripts combined with localization of proteins in whole-mount embryos. *BMC Biol.*, **12**, 55. 55-014-0055-7.
87. Eimon, P.M. (2014) Studying apoptosis in the zebrafish. *Methods Enzymol.*, **544**, 395–431.